









Hydrodynamics and survivability during post-main-sequence planetary engulfment

RICARDO YARZA ^{1,2,*} NAELA B. RAZO-LÓPEZ,¹ ARIADNA MURGUIA-BERTHIER ^{1,3,†} ROSA WALLACE EVERSON ^{1,‡}
ANDREA ANTONI ^{4,‡} MORGAN MACLEOD ⁵ MELINDA SOARES-FURTADO ^{6,†} DONGWOOK LEE ⁷ AND
ENRICO RAMIREZ-RUIZ ¹

¹Department of Astronomy and Astrophysics, University of California, Santa Cruz, CA 95064, USA

²Texas Advanced Computing Center, University of Texas, Austin, TX 78759, USA

³Center for Interdisciplinary Exploration and Research in Astrophysics (CIERA), 1800 Sherman Ave., Evanston, IL 60201, USA

⁴Department of Astronomy, University of California, Berkeley, CA 94720, USA

⁵Center for Astrophysics, Harvard & Smithsonian, 60 Garden Street, Cambridge, MA 02138, USA

⁶Department of Astronomy, University of Wisconsin-Madison, 475 N. Charter St., Madison, WI 53703, USA

⁷Department of Applied Mathematics and Statistics, University of California, Santa Cruz, CA 95064, USA

ABSTRACT

The engulfment of substellar bodies (SBs, such as brown dwarfs and planets) by giant stars is a possible explanation for rapidly rotating giants, lithium-rich giants, and the presence of SBs in close orbits around subdwarfs and white dwarfs. We simulate the flow in the vicinity of an engulfed SB in three-dimensional hydrodynamics. We model the SB as a rigid body with a reflective surface because it cannot accrete. This reflective boundary changes the flow morphology to resemble that of engulfed compact objects with outflows. We measure the drag coefficients for the ram pressure and gravitational drag forces acting on the SB, and use them to integrate its trajectory inside the star. We find that engulfment can increase the luminosity of a $1M_{\odot}$ star by up to a few orders of magnitude. The time for the star to return to its original luminosity is up to a few thousand years when the star has evolved to $\approx 10R_{\odot}$ and up to a few decades at the tip of the red giant branch. No SBs can eject the envelope of a $1M_{\odot}$ star before it evolves to $\approx 10R_{\odot}$, if the orbit of the SB is the only energy source contributing to the ejection. In contrast, SBs as small as $\approx 10M_{\text{Jup}}$ can eject the envelope at the tip of the red giant branch. The numerical framework we introduce here can be used to study planetary engulfment in a simplified setting that captures the physics of the flow at the scale of the SB.

1. INTRODUCTION

Common-envelope evolution (hereafter CEE; Paczynski 1976) is a process in which a star engulfs a companion (substellar or otherwise). The known planetary system architectures imply that a large fraction of planets and brown dwarfs (hereafter substellar bodies, SBs) will eventually undergo CEE (Villaver & Livio 2009; Mustill & Villaver 2012; Nordhaus & Spiegel 2013; Schlaufman & Winn 2013; Sun et al. 2018). Throughout this work, we will refer to CEE between a star and an SB as “planetary engulfment,” and use “CEE” for the more general interaction between a star and a companion of any mass.

Planetary engulfment is a possible explanation for several unsolved problems in stellar and planetary system evolution. Observations have found SBs in close orbits around

subdwarfs and white dwarfs (Schmidt et al. 2005; Littlefair et al. 2006; Maxted et al. 2006; Littlefair et al. 2007; Silvestri et al. 2007; Littlefair et al. 2008; Geier et al. 2009; Charpinet et al. 2011; Breedt et al. 2012; Casewell et al. 2012; Liu et al. 2012; Rebassa-Mansergas et al. 2012; Beuermann et al. 2013; Steele et al. 2013; McAllister et al. 2015; Almeida et al. 2017; Schaffenroth et al. 2015; Parsons et al. 2017; Pala et al. 2018; Casewell et al. 2020; Vanderburg et al. 2020; Schaffenroth et al. 2021; van Roestel et al. 2021, for a summary see Kruckow et al. 2021). These systems might have reached their current orbital configurations dynamically through the Kozai–Lidov mechanism (Kozai 1962; Fabrycky & Tremaine 2007; Katz et al. 2011; Naoz et al. 2012; Socrates et al. 2012; Shappee & Thompson 2013; Muñoz & Petrovich 2020; O’Connor et al. 2021) or via an engulfment phase in which the SB ejected the envelope of the star that engulfed it (Livio & Soker 1984; Nelemans & Tauris 1998; Lagos et al. 2021; Merlov et al. 2021; Zorotovic & Schreiber 2022). During engulfment, orbital energy dissipation shrinks the orbit of the system significantly. Even if the SB does not survive, engulfment might result in an isolated white dwarf with \gtrsim MG magnetic fields (Nordhaus et al. 2011; Guidarelli et al. 2019).

Corresponding author: Ricardo Yarza
ryarza@ucsc.edu

* NASA FINESST Fellow
Frontera Computational Science Fellow

† NASA Hubble Fellow

‡ NSF Graduate Research Fellow

Engulfment could explain observations of anomalous rotation among some giant stars. During engulfment, the SB transfers the angular momentum of its orbit into the stellar envelope, resulting in either enhanced or reduced rotation, depending on the alignment of the angular momentum vectors of the star and the orbit. Engulfment can speed up the surface of giant stars up to the observed values, and even up to a significant fraction of their critical speeds (Peterson et al. 1983; Soker 1998; Siess & Livio 1999; Zhang & Penev 2014; Privitera et al. 2016a,b; Qureshi et al. 2018; Stephan et al. 2020).

While the stellar surface abundance of the ${}^7\text{Li}$ isotope generally decreases throughout stellar evolution (Bodenheimer 1965; Deliyannis et al. 2000; Piau & Turck-Chièze 2002; Baumann et al. 2010; Monroe et al. 2013; Meléndez et al. 2014; Carlos et al. 2016, 2019; Soares-Furtado et al. 2021), dropping significantly at the onset of the first dredge-up phase, $\approx 1\%$ of giants have abundances ≥ 1.5 dex (e.g., Wallerstein & Sneden 1982; Brown et al. 1989; Balachandran et al. 2000; Charbonnel & Balachandran 2000; Reddy & Lambert 2005; Carlberg et al. 2010; Charbonnel & Lagarde 2010; Kumar et al. 2011; Martell & Shetrone 2013; Adamów et al. 2014, 2015; Yan et al. 2018; Li et al. 2018; Deepak & Reddy 2019; Gao et al. 2019; Singh et al. 2019). Moreover, $\approx 6\%$ of these ${}^7\text{Li}$ -rich giants exceed the meteoritic abundance of 3.3 dex, indicating that additional ${}^7\text{Li}$ must have been generated or deposited within them (Balachandran et al. 2000; Zhou et al. 2019; Singh et al. 2019). The engulfment of SBs is a possible explanation for high surface ${}^7\text{Li}$ abundances (Sandquist et al. 1998; Siess & Livio 1999; Sandquist et al. 2002; Aguilera-Gómez et al. 2016a,b; Soares-Furtado et al. 2021) because SBs do not reach the requisite temperatures to burn their primordial ${}^7\text{Li}$. However, there are other pathways for lithium enrichment, such as the Cameron & Fowler (1971) mechanism, which acts after the early red giant branch (RGB). The existence of these different pathways makes it harder to identify the source of enrichment for stars after the early RGB. Infrared excess is a potential indicator of stellar mass loss from engulfment, and evolved stars with infrared excess tend to have increased ${}^7\text{Li}$ and rotation rates (Mallick et al. 2022).

Several analytical studies (Metzger et al. 2012; Yamazaki et al. 2017; Jia & Spruit 2018) have focused on planetary engulfment by main-sequence (MS) or pre-main-sequence stars, where envelope ejection is unlikely because of the high gravitational binding energy. As for post-MS planetary engulfment, early analytical estimates (Nelemans & Tauris 1998; Livio & Soker 1984) suggest that SBs with masses¹ $\lesssim 10M_{\text{Jup}}$ cannot unbind the stellar envelope. Staff et al. (2016) simulated the engulfment of a massive planet by stars in the RGB and AGB using 3D hydrodynamics. However, their results regarding envelope ejection were limited by numerical resolution. Overall, planetary engulfment remains a relatively unexplored problem in the context of hydrodynamical simulations.

¹ We use the International Astronomical Union nominal values for solar system constants (Prša et al. 2016).

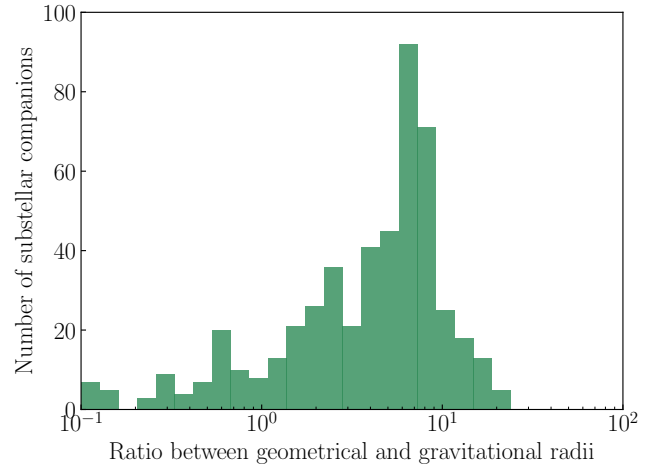


Figure 1. Distribution of exoplanets more massive than Jupiter (NASA Exoplanet Archive 2022) over the ratio of their geometrical and gravitational radii at the onset of engulfment, assuming they are engulfed at their current separations. Since tidal decay will lead to the engulfment of planets at smaller orbital separations than their current ones, this value is likely a lower limit. The geometrical radii are larger for 82% of these exoplanets.

Previous work on CEE has used the “wind tunnel” numerical formalism to study the flow in the vicinity of the engulfed companion, accounting for the density gradient in the stellar envelope (MacLeod & Ramirez-Ruiz 2015a,b; MacLeod et al. 2017; Murguia-Berthier et al. 2017; De et al. 2020; Everson et al. 2020). These density gradients change the flow morphology and give angular momentum to the gravitationally focused gas, thereby changing the drag forces on the companion. Most of this previous work has focused on interactions between an evolved star and a compact companion, for which gravitational drag dominates. For substellar companions, ram pressure drag might dominate, depending on stellar structure and on the companion. While some studies have recognized the importance of ram pressure (Staff et al. 2016; Jia & Spruit 2018), it has not yet been accounted for in detail.

The drag forces acting on the engulfed SB influence the dynamics of the orbital decay, the observational signatures associated with it, and ultimately whether the SB can survive engulfment. Here we study planetary engulfment using the wind tunnel numerical formalism.

In Section 2, we discuss the physical processes relevant to engulfment, particularly the relative importance of ram pressure and gravitational drag forces. In Section 3, we provide a brief review of the wind tunnel framework, and discuss its applicability and limitations in the context of planetary engulfment. We discuss flow morphology and drag coefficients in Section 4, and apply these results to planetary engulfment in Section 5. Section 6 summarizes our results.

2. PHYSICAL ASPECTS OF ENGLUFMENT

2.1. Gravitational and geometrical regimes

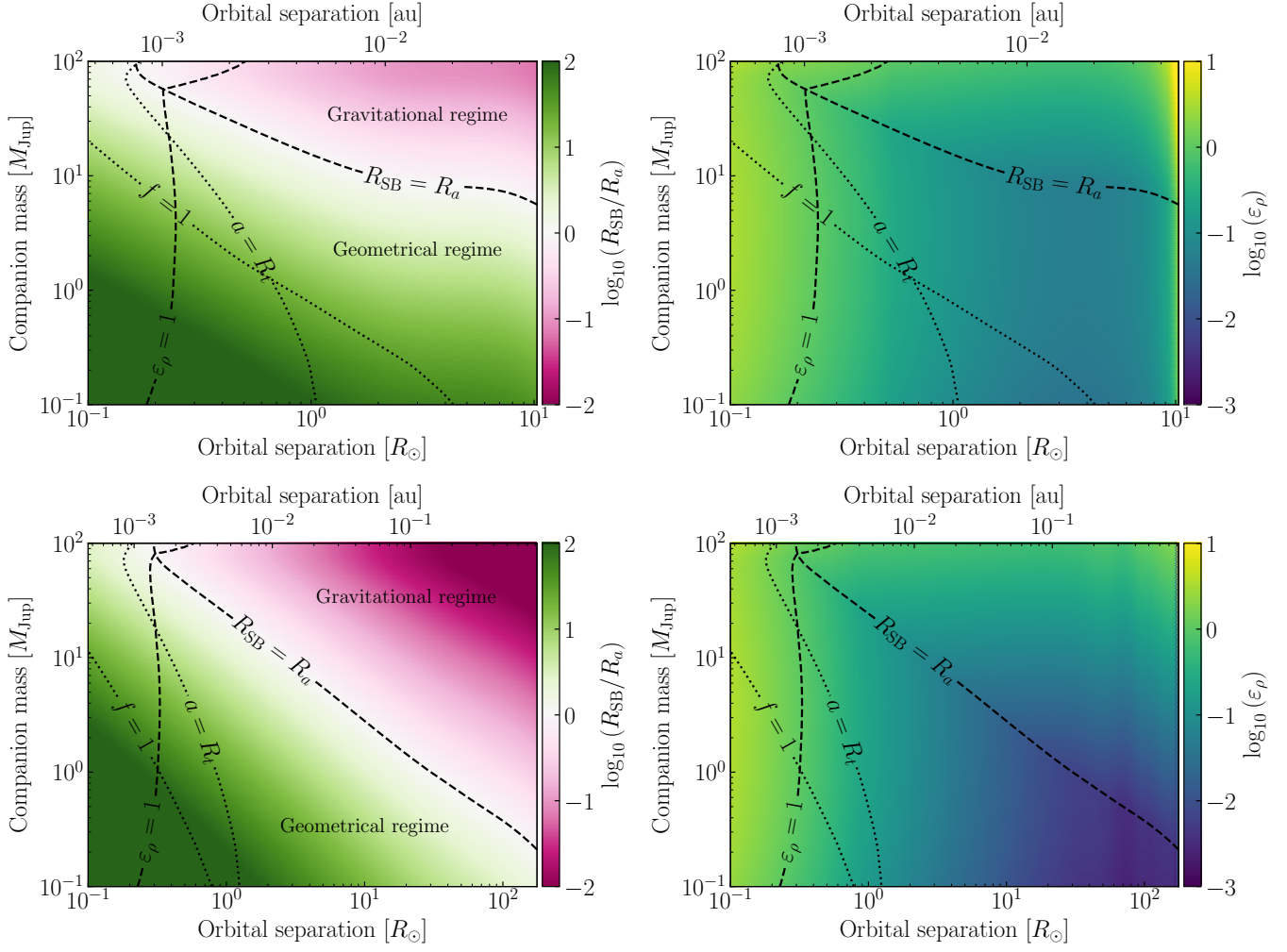


Figure 2. Dimensionless flow parameters (left: ratio between geometrical and gravitational radii, right: number of density scale heights across the larger radii) as a function of substellar body (SB) mass and position inside a model of the Sun evolved to $10R_{\odot}$ (top) and to the tip of the red giant branch (bottom). Dashed lines show the transition between geometrical and gravitational regimes, and between mild and strong density gradients. Dotted lines show estimates for SB disruption, either by tidal forces (when the separation equals the tidal radius R_t) or by ram pressure ($f = 1$, equation 4).

The interactions of an engulfed SB with the surrounding stellar material are gravitational (gravitational drag) and geometrical (ram pressure drag on the geometrical surface of the SB). Gravitational drag arises from gravitational focusing of material behind the SB; this focused material exerts a force against the direction of motion. An engulfed SB with mass M_{SB} travels relative to the surrounding gas at an orbital speed v_{orb} . Gas with an impact parameter smaller than the gravitational radius of the SB,

$$R_a = 2GM_{\text{SB}}/v_{\text{orb}}^2, \quad (1)$$

will be gravitationally focused behind the SB. This gas will exert a force $F_g = \pi C_g R_a^2 \rho v_{\text{orb}}^2$ (Hoyle & Lyttleton 1939; Bondi & Hoyle 1944; Bondi 1952), where G is the gravitational constant (we use the value given in Tiesinga et al. 2021), ρ is the envelope mass density, and C_g is a dimensionless coefficient of order unity. On the other hand, the pressure field

at the surface of the SB will exert a ram pressure force of the form $F_p = \pi C_p R_{\text{SB}}^2 \rho v_{\text{orb}}^2$, where R_{SB} is the geometrical radius of the SB, and C_p is a dimensionless coefficient of order unity.

Drag forces are approximately equal to the momentum per unit time passing through the cross-section for the corresponding interaction (geometrical or gravitational). The ratio between ram pressure and gravitational forces is therefore equal to the ratio of the cross-sections, $(R_{\text{SB}}/R_a)^2$, or equivalently the ratio $(v_{\text{orb}}/v_{\text{esc,SB}})^2$, where $v_{\text{esc,SB}} = \sqrt{2GM_{\text{SB}}/R_{\text{SB}}}$ is the escape velocity from the SB.

CEE studies have dealt almost exclusively with the engulfment of a compact object, such as a neutron star or black hole, in which case the interactions between the companion and the stellar material are mostly gravitational. Figure 1 shows the ratio between geometrical and gravitational cross-sections at the onset of engulfment for the known exoplanets, assuming

they are engulfed at their current orbital separations. Planets are likely to be engulfed at separations smaller than their current separations as a result of tidal decay. Since the Keplerian speed is greater at smaller separations, the gravitational radii of planets is likely to be smaller at engulfment than it is today, and more planets will be in the geometrical regime at the onset of engulfment. Equivalently, planets engulfed at earlier stages of stellar evolution are more likely to be in the geometrical regime, because they must orbit their host star more closely to be engulfed during earlier stages.

Figure 2 shows the same ratio as Figure 1, but as a function of SB mass and position inside a M_\odot star evolved to $10R_\odot$ (top panel) and at the tip of the RGB (bottom panel). We computed the properties of this star using the Modules for Experiments in Stellar Astrophysics (MESA, Paxton et al. 2011). As the SB dives deeper into the envelope, its interactions with the gas become increasingly geometrical because the Keplerian speed increases inwards. While it is possible for the Keplerian speed to decrease inwards if the enclosed mass profile is sufficiently steep, the post-MS envelopes we consider here are extended enough that the Keplerian speed always increases inwards. Therefore, interactions between the SB and the surrounding material become increasingly geometrical throughout engulfment.

Figure 2 also shows that more massive SBs tend to be deeper in the gravitational regime. Between $10^{-1}M_{\text{Jup}}$ and 10^2M_{Jup} , SB radius varies only between $0.7R_{\text{Jup}}$ and $1.2R_{\text{Jup}}$ (we determine the radius of each SB using the mass-radius relations from Fortney et al. 2007 and Chabrier et al. 2009). As M_{SB} increases, R_{SB} remains approximately constant, but R_a is proportional to M_{SB} (equation 1), so R_{SB}/R_a is approximately inversely proportional to M_{SB} .

The right panels in Figure 2 shows the number of density scale heights across the SB,

$$\varepsilon_\rho \equiv \max(R_{\text{SB}}, R_a) / H_\rho, \quad (2)$$

where the density scale height $H_\rho \equiv -\rho / (d\rho/dr)$. The dimensionless density gradient ε_ρ quantifies the heterogeneity of the flow at the scale of the SB. Engulfed SBs typically experience mild ($0 \leq \varepsilon_\rho \lesssim 1$) density gradients.

2.2. Destruction of the substellar body

The SB will be tidally disrupted when

$$\langle \rho_{\text{enc}} \rangle = \langle \rho_{\text{SB}} \rangle, \quad (3)$$

where $\langle \rho_{\text{enc}} \rangle$ is the average density of the material enclosed by the SB's orbit, and $\langle \rho_{\text{SB}} \rangle$ is the average density of the SB. This criterion is equivalent to the orbital separation being equal to the tidal radius of the SB.

We estimate the SB will be disrupted by ram pressure when the kinetic energy per unit volume of the incoming flow equals the binding energy per unit volume of the SB, i.e., when (Jia & Spruit 2018)

$$f \equiv \frac{\rho v_{\text{orb}}^2}{\langle \rho_{\text{SB}} \rangle v_{\text{esc,SB}}^2} = 1. \quad (4)$$

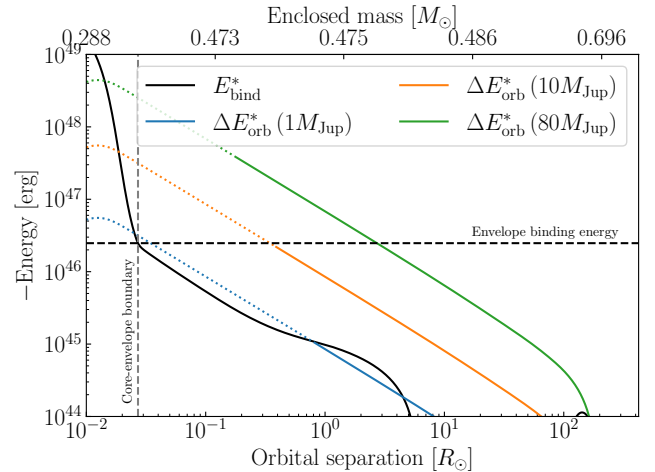


Figure 3. Comparison between the binding energy of exterior material E_{bind}^* and orbital energy ΔE_{orb}^* deposited by substellar bodies (SBs) of different masses, as a function of position inside a model of the sun at the tip of the red giant branch. Orbital energy deposition lines turn dashed at the estimated destruction point for each SB.

As shown in Figure 2, tidal disruption is the dominant destruction process for most SBs. Ram pressure will disrupt SBs with masses $\lesssim 1M_{\text{Jup}}$ engulfed early in the red giant branch.

2.3. Envelope ejection

We use the standard energy formalism of CEE (van den Heuvel 1976; Webbink 1984) to estimate analytically whether envelope ejection is possible. In this formalism, an engulfed companion will eject material exterior to the orbital separation r if the binding energy of that material is smaller in magnitude than the change in orbital energy of the SB, i.e., $|\Delta E_{\text{orb}}^*| > |E_{\text{bind}}^*|$, where

$$\Delta E_{\text{orb}}^* = -\frac{GM_{\text{enc}}M_{\text{SB}}}{2r} + \frac{GM_{\text{enc},0}M_{\text{SB}}}{2r_0}, \quad (5)$$

$$E_{\text{bind}}^* = \int_{M_{\text{enc}}}^{M_{\text{enc},0}} \left(-\frac{GM'_{\text{enc}}}{r} + u \right) dM'_{\text{enc}}. \quad (6)$$

Here, u is the specific internal energy, M_{enc} is the enclosed mass at orbital separation r , and the 0 subscript refers to values at the initial time $t = 0$. These two equations neglect the binding energy between the star and the SB; at the low mass ratios we study here, the envelope is much more bound to the core than to the SB, so we omitted these terms for conciseness and readability. Figure 3 compares E_{bind}^* for a MESA model of the Sun at the tip of the RGB to ΔE_{orb}^* for SBs of several masses. We define the core-envelope boundary as the radial coordinate at which the hydrogen mass fraction is 1/10. We consider envelope ejection to be possible if the $|\Delta E_{\text{orb}}^*|$ is at any point (before destruction of the SB) above the value of the $|E_{\text{bind}}^*|$ curve at the core-envelope boundary. The Figure shows this value as a horizontal line labeled “envelope binding energy.” This prescription assumes that energy can be efficiently distributed in the envelope, so that energy deposited

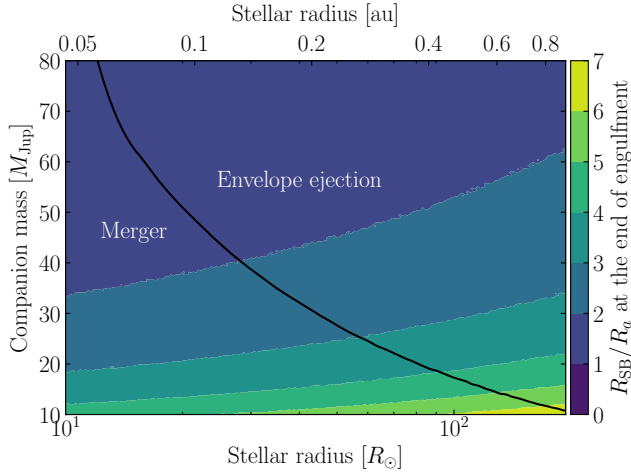


Figure 4. Ratio of geometrical and gravitational cross-sections at the point of envelope ejection or SB destruction, as a function of stellar radius and SB mass. The dashed line shows the minimum mass required to eject the envelope according to the standard energy formalism. When engulfment ends, either by destruction of the SB or envelope ejection, all SBs are in the geometrical regime.

at r can eject material at $r' < r$. As we will see (Figure 6), the SB significantly disturbs material within a few $\max(R_{\text{SB}}, R_a)$ of its current location. Tidal forces destroy massive SBs at orbital separations comparable to their size (see the lines for $10M_{\text{Jup}}$ and $80M_{\text{Jup}}$ in Figure 3), so we expect at least the energy they deposit near the destruction point to reach the core-envelope boundary.

According to the standard energy formalism, objects with masses $\gtrsim 10M_{\text{Jup}}$ might eject the envelope of a Sun-like star at the tip of the red giant branch. Figure 4 shows R_{SB}/R_a at the location of either SB destruction or envelope ejection, as a function of SB mass and stellar radius. The solid line shows the minimum SB mass required to eject the envelope. The star expands throughout the RGB, so its binding energy decreases and envelope ejection by smaller SBs becomes possible. No companion with mass $< 80M_{\text{Jup}}$ can eject the envelope of an M_{\odot} star early in the RGB. All SBs are in the geometrical regime when they are destroyed or when they eject the envelope, highlighting the need for numerical models of ram pressure drag.

2.4. Orbital decay timescales

The rate of orbital energy dissipation is the work per unit time done by the drag forces, so the orbital decay timescale for ram pressure drag is

$$\tau_{\text{insp,p}} \approx \frac{E_{\text{orb}}}{\dot{E}_{\text{orb}}} = \frac{GM_{\text{SB}}M_{\text{enc}}}{2aF_p v_{\text{orb}}} = \frac{GM_{\text{enc}}M_{\text{SB}}}{2\pi C_p a R_{\text{SB}}^2 v_{\text{orb}}^3 \rho}, \quad (7)$$

and for gravitational drag

$$\tau_{\text{insp,g}} \approx \frac{GM_{\text{SB}}M_{\text{enc}}}{2aF_g v_{\text{orb}}} = \left(\frac{M_{\text{enc}}}{M_{\text{SB}}}\right) \frac{v_{\text{orb}}}{8\pi G C_g a \rho}. \quad (8)$$

In the geometrical regime, the orbits of more massive SBs decay more slowly because they experience approximately the same force, but have larger inertia. As before, radius is almost constant in mass between $1M_{\text{Jup}}$ and $100M_{\text{Jup}}$, so the change in the geometrical orbital decay timescale as a result of changes in SB radius is negligible. In the gravitational regime, however, the orbits of more massive SBs decay faster because the gravitational cross-section scales as the square of their mass, overcoming the inertial term. Whether the orbital decay timescale is equation 7 or equation 8 depends on R_{SB}/R_a at the onset of engulfment.

Tides might dominate the orbital decay of the companion in the outer envelope (Stephan et al. 2020), but we do not account for them here. Additionally, the drag orbital decay timescales are sensitive to the density of the stellar envelope at the onset of engulfment because the object will spend most of its time in the outer envelope, where drag forces are smaller. The orbital and tidal evolution during the post-main-sequence set the initial conditions for engulfment. Hydrodynamical simulations (Staff et al. 2016) show that the star will overflow its Roche lobe. Our calculations neglect these effects by using the unperturbed stellar structure throughout engulfment.

We expect the orbits of all SBs engulfed near the tip of the RGB to decay on a timescale comparable to Equation 8 because they are in the gravitational regime at the onset of engulfment (see Figure 2). In earlier stages of stellar evolution, however, less massive SBs can be in the geometrical regime at the onset of engulfment, and more massive SBs in the gravitational regime. Since the gravitational and ram pressure timescales have opposite scaling in mass, the orbits of intermediate-mass SBs will decay the slowest in these stars (see Appendix A).

3. WIND TUNNEL NUMERICAL FRAMEWORK

Global simulations of planetary engulfment that account for changes in the internal structure of the post-MS star and the SB are computationally challenging and expensive because they involve two vastly different scales. The scale of the flow in the vicinity of the SB is $\approx \max(R_{\text{SB}}, R_a) \approx R_{\text{Jup}}$, while the scale of the orbit and the star is $\approx 1 \text{ au} \approx 10^3 R_{\text{Jup}}$. This disparity of scales motivates isolating the processes occurring at each scale, not only for computational feasibility and accuracy, but also to understand the role of each of these processes and eventually the interplay between the processes at different scales. Here we perform simulations of the flow within a few $\max(R_{\text{SB}}, R_a)$ of the SB. We aim to understand the morphology of the flow in the vicinity of the SB, and the forces acting on it. Measurements of these forces allow numerical integration of the equation of motion of the SB inside the star. This approach allows inexpensive yet reasonably accurate exploration of a much larger region of parameter space.

We use the “wind tunnel” numerical setup (MacLeod et al. 2017), illustrated in Figure 5. We simulate a local domain in the frame of the engulfed SB, and we supply a time-independent “wind” from the $-\hat{x}$ direction. The flow morphology (and therefore the drag coefficients) is uniquely determined by a set of dimensionless parameters: the mass

ratio $q \equiv M_{\text{SB}}/M_{\text{enc}}$, the dimensionless density gradient ε_ρ (equation 2), the mach number \mathcal{M} , and the ratio between geometrical and gravitational radii R_{SB}/R_a . The equation of hydrostatic equilibrium for the envelope (MacLeod et al. 2017) relates these parameters as

$$\min\left(1, \frac{R_a}{R_{\text{SB}}}\right) \varepsilon_\rho = \frac{2q}{(1+q)^2} f_k^{-4} \mathcal{M}^2, \quad (9)$$

where f_k is the ratio between the speed of the companion relative to the surrounding material and the Keplerian speed. Equation 9 implies three dimensionless parameters are enough to uniquely specify the flow morphology; for most of this work we use the set $(q, \varepsilon_\rho, R_{\text{SB}}/R_a)$. Since the drag coefficients are a function of only these dimensionless parameters, a single simulation can determine the drag for a variety of physical systems. The drag coefficients do not depend on dimensional quantities that set the scale of the system. These quantities do not change the flow morphology, and the total drag scales with them in known ways (for example, linearly, in the case of the density). For simplicity, we set the density at $y = 0$ to 1 g cm^{-3} , and the wind speed to 1 cm s^{-1} . We set the pressure at $y = 0$ so that the flow has the Mach number implied by hydrostatic equilibrium and the rest of the dimensionless parameters.

After computing the flow properties at $y = 0$, we integrate the equations of hydrostatic equilibrium for a massless atmosphere up to the boundaries in the $\pm \hat{y}$ directions. In the $-\hat{y}$ direction, we extend hydrostatic equilibrium to the ghost zones. We add the gravitational field of the enclosed stellar mass so that the gas remains in hydrostatic equilibrium in the absence of external forces. The external force in our simulations, leading to the deflection of the gas, is the gravity of the SB. For all other boundaries, we use outflow boundary conditions, in which gas can leave the domain but not enter it. For more details, see MacLeod et al. (2017). The numerical setup is publicly available (see Appendix C).

We set $f_k = 1$, thereby assuming a circular orbit and no corotation between the star and the SB. During the post-main-sequence, synchronization tides shrink the orbit of the companion and transfer its angular momentum into the star. Small SBs do not have enough orbital angular momentum to bring the star into corotation (equality of the orbital and rotational periods of the star), leading to orbital decay through the Darwin (1879) instability. The ratio between rotational and orbital periods at the onset of the engulfment of a Jupiter-like planet by a Sun-like host star evolved to $0.05 R_\odot$ is ≈ 0.2 (Gallet et al. 2017); for gas giant planets engulfed by a $1.5 M_\odot$ host star, this ratio is $\lesssim 0.3$ (Table A.1 of Privitera et al. 2016b). More massive SBs, such as brown dwarfs, will enhance stellar rotation more.

In the wind tunnel framework, the density gradient (pointing in the $-\hat{y}$ direction) and the velocity of the stellar material in the frame of the SB (pointing in the \hat{x} direction) are perpendicular. This configuration doesn't accurately represent the flow around the SB when its orbit is eccentric. Tides significantly lower the orbital eccentricity of closely orbiting planets

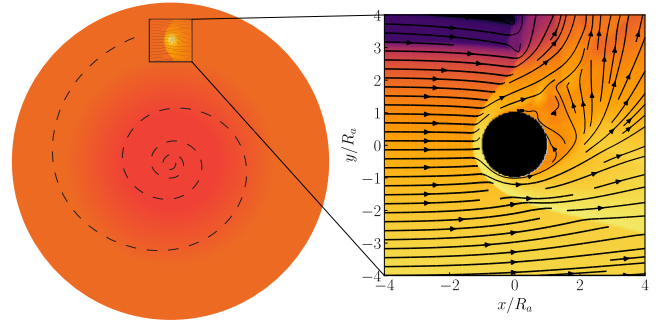


Figure 5. Schematic of the wind tunnel numerical setup. Left: substellar body (SB) embedded in the envelope of a giant star, with an orbital decay trajectory shown as a dashed line. Right: density slice and velocity streamlines in a wind tunnel simulation of the embedded object. The wind velocity and density gradient point in the \hat{x} and $-\hat{y}$ directions, respectively. The orbital speed is higher than the local sound speed, so the object will drive a shock as it moves through the stellar envelope.

throughout stellar evolution, while the eccentricity of distant planets remains roughly constant (see Figure 8 of Villaver et al. 2014). The average eccentricity of the known exoplanets more massive than Jupiter around stars between $0.7 M_\odot$ and $1.5 M_\odot$ is ≈ 0.2 (NASA Exoplanet Archive 2022). As a result of tides, these planets will likely be engulfed in orbits more circular than their current ones. However, there is theoretical and observational evidence for a transient population of exoplanets orbiting evolved stars at moderate eccentricity (Villaver et al. 2014; Grunblatt et al. 2022), whose orbits decay before they circularize.

This framework also neglects the curvature of the velocity field within the domain. This approximation is valid when the half-length of the domain $L_{\text{domain}}/2$ is much smaller than the orbital separation r . We set the domain length to $10 \max(R_{\text{SB}}, R_a)$. In the geometrical regime, the condition $L_{\text{domain}}/2 < r$ reduces to $R_{\text{SB}}/R_a < (1 + q^{-1})/10$. In the gravitational regime, it reduces to $q < 1/9$. Figure 8 shows these constraints.

We wrote this numerical framework as a setup for the FLASH (Fryxell et al. 2000; Dubey et al. 2014, 2015) code. It uses FLASH to solve the equations of inviscid hydrodynamics on a Cartesian mesh with adaptive mesh refinement. We use an ideal gas equation of state $P = (\gamma - 1)u$, where P is the pressure, γ the ratio of specific heats (which we take to be $5/3$), and u is the internal energy per unit volume. The base resolution of our simulations is 160 cells per dimension. We use adaptive mesh refinement with a criterion based on proximity to the surface of the SB; we choose the maximum level of refinement such that there are always ≈ 60 cells across the SB. See Appendix A.1 for hydrodynamics convergence tests.

3.1. Model for the substellar body

Previous wind tunnel CEE simulations between extended stars and compact objects have modeled the compact object as a numerical ‘‘sink.’’ Inside the sink, the simulation multiplies

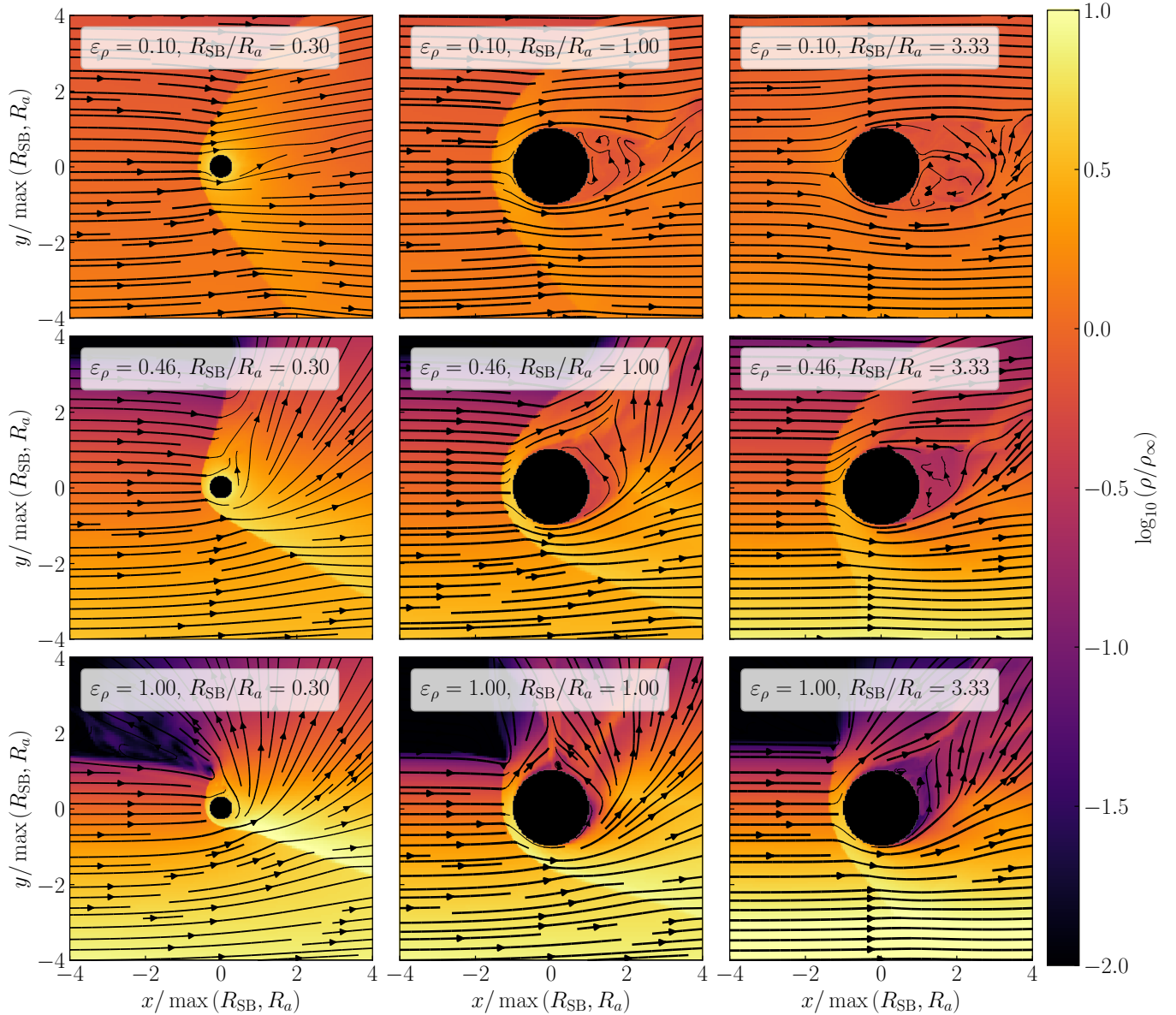


Figure 6. Density (in units of upstream density at $y = 0$, ρ_∞) slices in wind tunnel simulations, for several values of the ratio between geometrical and gravitational radii R_{SB}/R_a , and the number of density scale heights per $\max(R_{\text{SB}}, R_a)$. These slices are at $t = 20 \max(R_{\text{SB}}, R_a) / v_{\text{orb}}$, where v_{orb} is the upstream gas speed. At low R_{SB}/R_a , a spherically symmetric envelope of material that cannot be accreted forms around the SB, suppressing ram pressure drag. At high R_{SB}/R_a , a vacuum forms behind the SB, increasing ram pressure drag and suppressing gravitational drag. An animated version of this figure is available in the HTML version of the article. The animation shows the time evolution of the density slices from $t = 0$ to $t = 20 \max(R_{\text{SB}}, R_a) / v_{\text{orb}}$.

fluid variables by a small number, creating a numerical vacuum that emulates accretion of the surrounding material onto the object. In real systems, these objects accrete because the material accumulating around them is hot and dense enough to cool via neutrino emission (MacLeod & Ramirez-Ruiz 2015b; Fragos et al. 2019). There is no such cooling channel for material near the surface of the SB, and the gas is too optically thick to cool radiatively. The timescale over which radiation will carry energy through the optically thick surrounding material, allowing it to be accreted, is much longer

than the orbital decay timescale. We therefore model the SB as a rigid body with a reflective surface. We use FLASH’s unsplit hydrodynamics solver, which is based on the unsplit magnetohydrodynamics solver (Lee 2013). The code applies the reflective boundary condition at the surface of the rigid body, i.e., in the rigid body cells adjacent to the fluid cells. The reflective boundary implementation in FLASH requires a Courant–Friedrichs–Lewy (CFL) number ≤ 0.3 for numerical stability because the reconstruction order near the boundary is lower.

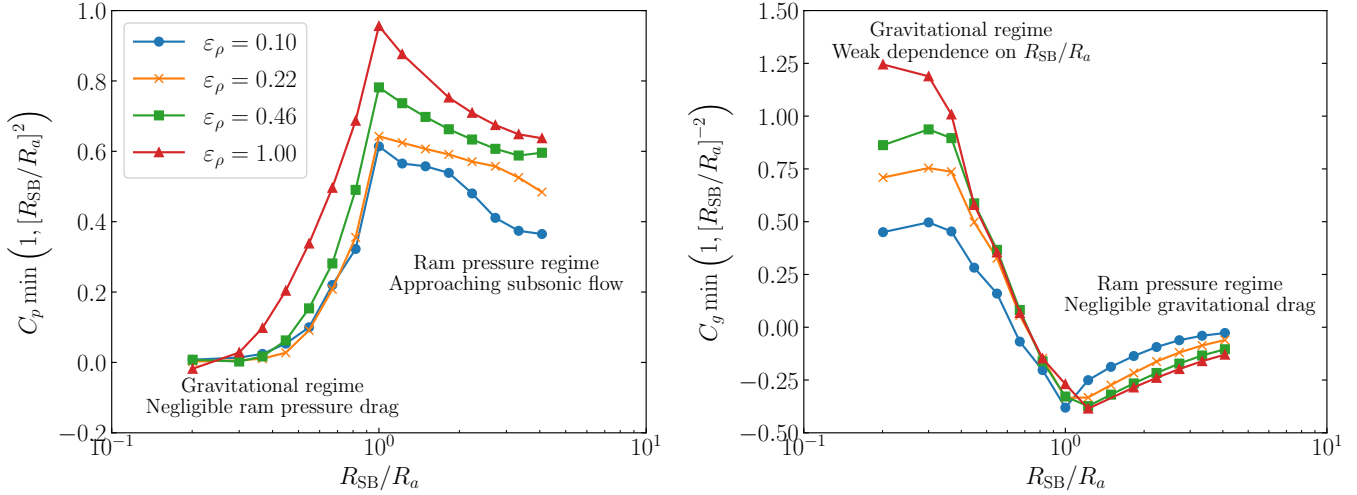


Figure 7. Ram pressure (left) and gravitational (right) drag coefficients for a set of simulations with mass ratio $q = 2.15 \times 10^{-2}$, as a function of the ratio between geometrical and gravitational radii, R_{SB}/R_a . Each line corresponds to a different dimensionless gradient ε_ρ . The drag coefficients depend on R_{SB}/R_a most strongly during the transition regime $R_{\text{SB}} \sim R_a$, then have a weaker dependence until the mach number approaches (and goes below) unity.

During the engulfment of a compact object by a giant star, the geometrical size of the object is negligible ($R_{\text{SB}} \ll R_a$), whereas an engulfed SB can have $R_{\text{SB}} \gtrsim R_a$. When the radius of the “sink” object is $\gtrsim 0.2R_a$, the shock morphology changes into a “tail shock” that trails the path of the object (Figure 10 in Ruffert & Arnett 1994). As we will see (Figure 6), the reflective boundary prevents this change in morphology. These qualitative differences motivate modified wind tunnel simulations that more accurately represent how engulfed SBs interact with their surroundings, and the associated flow morphology and drag coefficients.

We do not model the internal structure of the SB, whose mass loss and deformation could affect the flow morphology around it, and the cross-section for interactions with its surroundings. Ram pressure will flatten the surface of the SB facing the incoming flow and compress the SB, making it harder to disrupt (Jia & Spruit 2018). Gradual ablation of the SB is unlikely to destroy the SB before “global” processes that act on its dynamical timescale (Passy et al. 2012; Jia & Spruit 2018), although the hydrodynamics of ablation in this context are uncertain. We discussed these global processes in Section 2.2; we evaluate their corresponding destruction criteria using only the unperturbed SB structure.

3.2. Drag force measurements

We measure the forces on the object when the simulation reaches steady state, which takes a few flow-crossing times $\tau_c = \max(R_a, R_{\text{SB}})/v_{\text{orb}}$. We measure the gravitational drag force by integrating the gravitational force of the surrounding density field up until $1.6 \max(R_{\text{SB}}, R_a)$, as in MacLeod et al. (2017). The ram pressure drag force is

$$\mathbf{F}_p = - \oint_S P d\mathbf{A}, \quad (10)$$

where $d\mathbf{A}$ is the area element and S is the surface of the SB. Our setup uses FLASH to solve the equations of inviscid hydrodynamics; while the discretization of the equations results in numerical viscosity, there is not a boundary layer around the SB, which could change the ram pressure drag and the viscous stresses acting on it. For the same reason we do not study the dependence of the ram pressure drag on the Reynolds number.

The coefficients measured from the steady state simulations are valid if the timescale over which the simulation reaches steady state is much shorter than the orbital decay timescale. For SBs dominated by ram pressure, whose orbital decay time is equation 7, $\tau_c/\tau_{\text{insp,p}} = \rho/\langle\rho_{\text{SB}}\rangle < \langle\rho_{\text{enc}}\rangle/\langle\rho_{\text{SB}}\rangle$, where the inequality holds because the density decreases monotonically with radius. This ratio is less than unity at the onset of engulfment; when it reaches unity, the core tidally disrupts the SB (equation 3). For SBs dominated by gravitational drag, $\tau_c/\tau_{\text{insp,g}} = (M_{\text{SB}}/M_{\text{enc}})^2 \rho/\langle\rho_{\text{enc}}\rangle < 1$.

4. FLOW MORPHOLOGY AND DRAG

4.1. The gravitational and geometrical regimes

Figure 6 shows steady state density slices of wind tunnel simulations with $q = 2.15 \times 10^{-2}$, at several R_{SB}/R_a and ε_ρ . At low R_{SB}/R_a (the leftmost column in the Figure), the SB gravitationally focuses gas as in the Bondi–Hoyle–Lyttleton formalism. However, since the SB cannot accrete, this focused material accumulates at its surface. The pressure force exerted by this material opposes the pressure force from material accumulated in front of the object a result of compression when the SB moves through the gas. The resulting pressure field at the surface of the object is spherically symmetric, suppressing ram pressure drag (Thun et al. 2016). As R_{SB}/R_a decreases, ram pressure drag becomes less important not only because

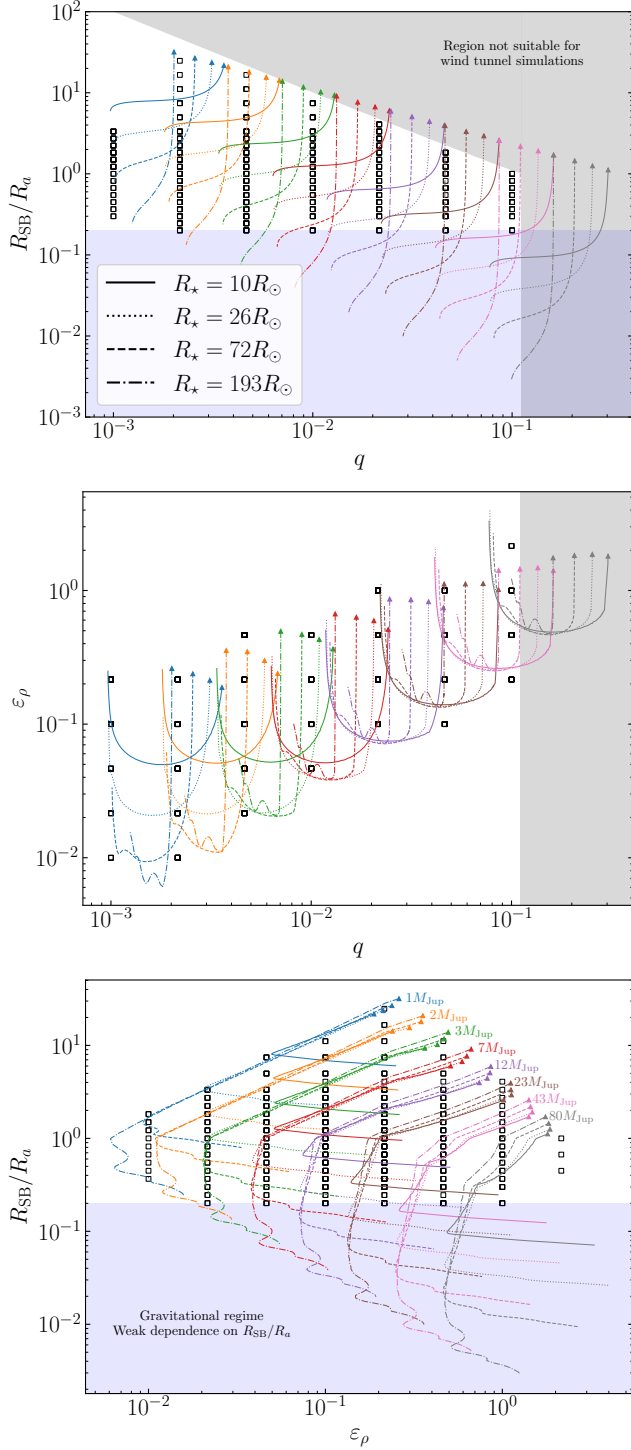


Figure 8. Trajectories in parameter space followed by substellar bodies (SBs) of varying masses after being engulfed by a $1M_{\odot}$ star at varying evolutionary stages. Each line style represents a different evolutionary stage (see legend on top panel), and each color represents an SB of a different mass (see inline labels on bottom panel). Each line starts at a radial coordinate $r = 0.9R_{*}$, and ends at the point of SB destruction, represented by a triangle. The squares represent the hydrodynamical simulations done in this work.

the geometrical cross-section decreases, but also because of morphological changes to the flow.

When $R_{\text{SB}} \sim R_a$, the gravity of the SB is not strong enough to deflect the surrounding material, and a low-density region forms behind the SB. The ram pressure force exerted by gas in front of the SB is now unopposed, and gravitational drag decreases significantly. When $R_{\text{SB}} \gg R_a$, the material in front of the SB dominates gravitational drag (as opposed to material behind the SB, as when $R_{\text{SB}} \ll R_a$), and the gravitational drag coefficient becomes negative. Similar results have been found for compact objects with outflows (Gruzinov et al. 2020; Li et al. 2020; Kaaz et al. 2022) and luminous planetesimals moving through a disk (Masset & Velasco Romero 2017; Masset 2017). In those settings, feedback from the object can interfere with the flow at impact parameters $\sim R_a$ that the SB would have gravitationally focused had there been no feedback. In our simulations, the rigidity of the SB and its reflective surface have this effect when $R_{\text{SB}} > R_a$.

Figure 7 shows the drag coefficients for the same set of simulation parameters as Figure 6. In the gravitational regime, the drag force is most naturally written as

$$\mathbf{F}_{\text{drag}} = -\pi\rho v^2 R_a^2 \left[C_g + \left(\frac{R_{\text{SB}}}{R_a} \right)^2 C_p \right] \hat{v}, \quad (11)$$

where \hat{v} is the unit vector in the direction of the SB’s velocity. On the other hand, in the geometrical regime

$$\mathbf{F}_{\text{drag}} = -\pi\rho v^2 R_{\text{SB}}^2 \left[C_p + \left(\frac{R_{\text{SB}}}{R_a} \right)^{-2} C_g \right] \hat{v}. \quad (12)$$

Equations 11 and 12 are equivalent, but it is often convenient to write the drag force in the functional form of the dominant source of drag, with a small correction term that accounts for the nondominant source of drag. The drag can be written as a combination of the previous two expressions,

$$\mathbf{F}_{\text{drag}} = -\pi\rho v^2 \max(R_{\text{SB}}, R_a)^2 (C_{p,\text{eff}} + C_{g,\text{eff}}) \hat{v}, \quad (13)$$

where

$$C_{p,\text{eff}} \equiv C_p \min \left(1, \left[\frac{R_{\text{SB}}}{R_a} \right]^2 \right), \quad (14)$$

$$C_{g,\text{eff}} \equiv C_g \min \left(1, \left[\frac{R_a}{R_{\text{SB}}} \right]^2 \right). \quad (15)$$

The primary motivation for writing the drag force this way is that the ratio between the “effective” coefficients equals the ratio between the drag forces. Additionally, when the flow converges to the geometrical regime, the effective gravitational drag coefficient approaches zero. The gravitational drag coefficient alone does not approach zero when $R_{\text{SB}} \gg R_a$ because in that limit the material in front of the SB dominates gravitational drag. Since larger SBs have more material in front of them, the gravitational force exerted by that material is larger. However, this gravitational drag force increases with R_{SB}/R_a

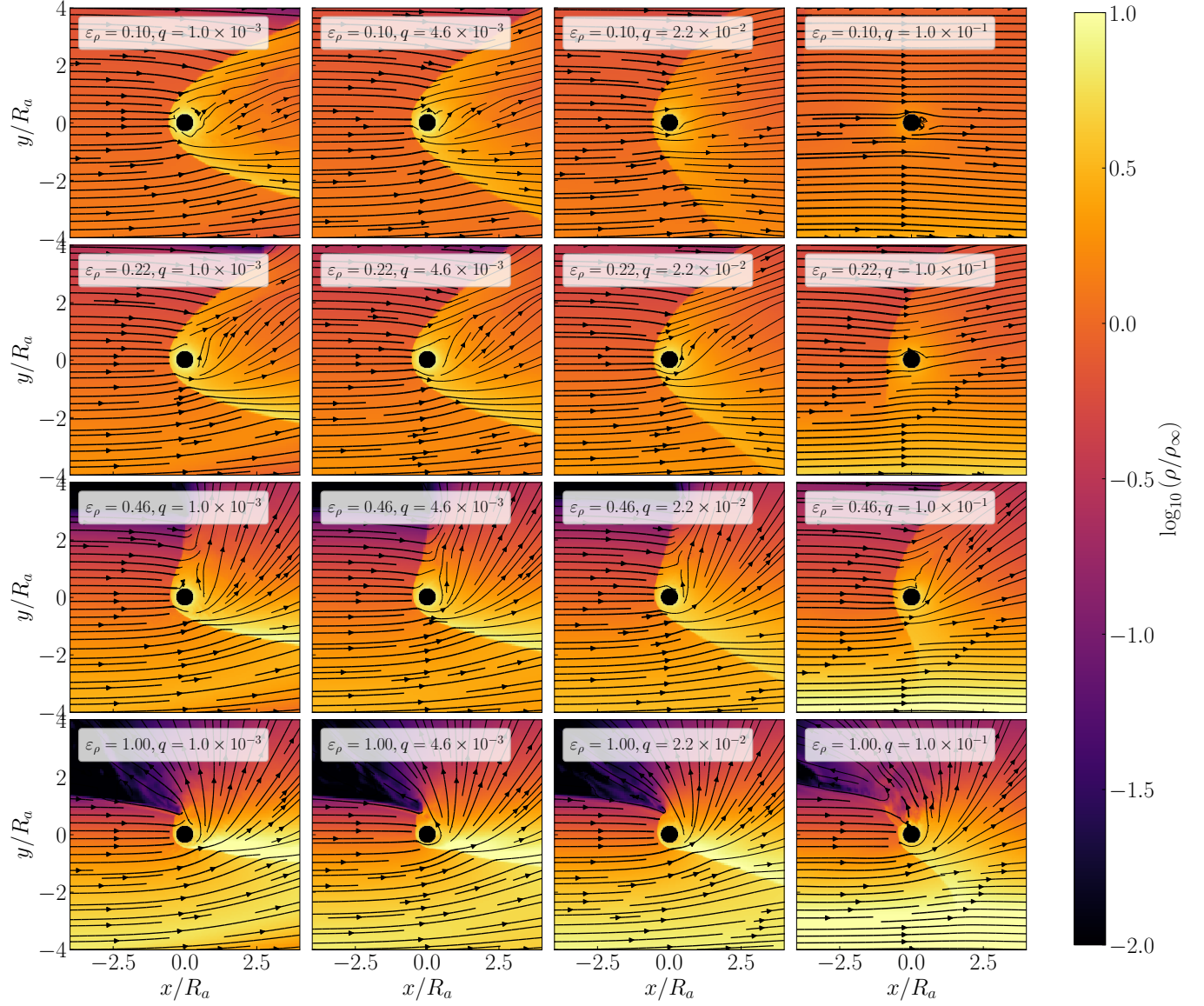


Figure 9. Density (in units of upstream density at $y = 0$, ρ_∞) in wind tunnel simulations as a function of space. Each panel shows a different combination of the dimensionless density gradient (ε_ρ), and the ratio between the mass of the substellar object and the mass enclosed by its orbit (q). The ratio between geometrical and gravitational radii is 0.3 in all panels. These slices are at $t = 20R_a/v_{\text{orb}}$, where v_{orb} is the upstream gas speed. Larger density gradients and Mach numbers result in higher drag coefficients. An animated version of this figure is available in the HTML version of the article. The animation shows the time evolution of the density slices from $t = 0$ to $t = 20R_a/v_{\text{orb}}$.

slower than quadratically, so gravitational drag becomes a smaller fraction of the total drag as R_{SB}/R_a increases.

Figure 7 shows that when $R_{\text{SB}} \lesssim 0.25$ the effective drag coefficients are independent of R_{SB}/R_a , so that

$$C_{g,\text{eff}} = C_g = C_g(q, \varepsilon_\rho), \quad (16)$$

$$C_{p,\text{eff}} = C_p (R_{\text{SB}}/R_a)^2 \approx 0. \quad (17)$$

On the other hand, the ram pressure drag coefficient depends on R_{SB}/R_a even when $R_{\text{SB}} \gg R_a$. This dependence can be understood from the equation of hydrostatic equilib-

rium, which when $R_{\text{SB}} > R_a$ reduces to

$$\frac{R_a}{R_{\text{SB}}} \varepsilon_\rho = \frac{2q}{(1+q)^2} f_k^{-4} \mathcal{M}^2. \quad (18)$$

At a fixed mass ratio q and dimensionless density gradient ε_ρ , the mach number $\mathcal{M} \propto (R_{\text{SB}}/R_a)^{-1/2}$. As R_{SB}/R_a increases, the mach number decreases, so the density discontinuity across the shock is smaller, reducing ram pressure drag. This gradual transition towards subsonic flow can be seen in the top row of Figure 6, from left to right. In the geometrical

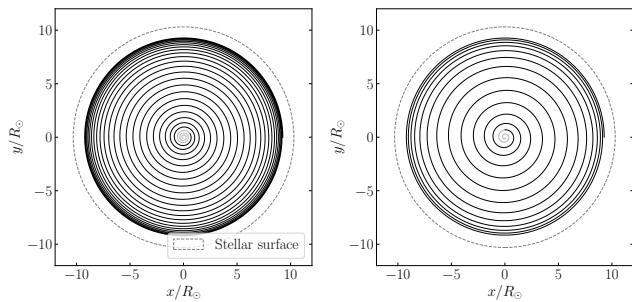


Figure 10. Orbital decay trajectory of a $1M_{\text{Jup}}$ planet inside a $1M_{\odot}$ star evolved to $10R_{\odot}$, as computed using analytical (left panel) and numerical (right panel) drag coefficients. Trajectories turn transparent at the estimated point of destruction. Orbital decay takes ≈ 24 d (a factor of ≈ 2 faster) when using numerical drag coefficients.

regime,

$$C_{g,\text{eff}} = C_g (R_a/R_{\text{SB}})^2 \approx 0, \quad (19)$$

$$C_{p,\text{eff}} = C_p = C_p(q, \varepsilon_\rho, R_{\text{SB}}/R_a). \quad (20)$$

4.2. Dependence on mass ratio and dimensionless density gradient

The dependence of the drag coefficients on the density gradient, the Mach number, and the mass ratio can be understood from the relationship between these parameters in hydrostatic equilibrium (Equation 9), and the flow morphology in Figure 9. Simulations with stronger density gradients have larger drag coefficients because the SB interacts with higher density gas (from deeper in the envelope) both geometrically and gravitationally. From hydrostatic equilibrium, increasing the mass ratio at a fixed Mach number will result in a stronger density gradient, and larger drag coefficients.

Similarly, at a given density gradient, larger Mach numbers result in a narrower shock opening angle, allowing focused material to accumulate closer to $y = 0$, increasing the horizontal component of the drag force and therefore the gravitational drag coefficient. Higher Mach numbers also result in increased gas compression in front of the SB, increasing the ram pressure drag coefficient. At fixed density gradient, increasing the Mach number requires decreasing the mass ratio, so increasing mass ratios reduce the drag coefficient.

5. APPLICATIONS TO PLANETARY ENGULFMENT

5.1. Parameter space for hydrodynamical simulations

Figure 8 shows the trajectories of engulfed SBs in parameter space, for several SB masses and stellar evolutionary stages. Each line style corresponds to a stellar evolutionary stage, and each color corresponds to an SB mass. Each line starts at a radial coordinate $r = 0.9R_*$ and ends at the point of SB destruction, represented by a triangle. This figure, as Figure 2, assumes SBs are in circular orbits throughout engulfment. The wind tunnel framework cannot simulate the region in parameter space where the domain size would be comparable to the orbital separation (the gray region in the top and

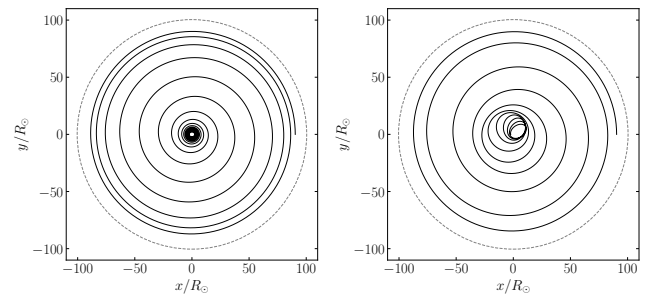


Figure 11. Orbital decay trajectory of a $80M_{\text{Jup}}$ brown dwarf inside a $1M_{\odot}$ star evolved to $100R_{\odot}$, as computed using analytical (left panel) and numerical (right panel) drag coefficients. For readability, we show the trajectories only down to an orbital separation of $2.5R_{\odot}$. While the orbital decay timescale is similar in both cases (≈ 1.3 yr), numerical drag coefficients result in a more eccentric orbit.

middle panels). We discussed this limitation quantitatively in Section 3.

The top panel shows that more massive SBs (those with higher q) are deeper in the gravitational regime, and that R_{SB}/R_a increases throughout engulfment. The destruction points for SBs with $q \gtrsim 5 \times 10^{-3}$ lie in a line; these SBs are destroyed by tidal disruption. From the definition of the tidal radius, tidal disruption will occur when the orbital separation $r = R_{\text{SB}}q^{-1/3}$. Under the assumption of circular orbits, $R_a = 2qr$. Combining these two equations, $R_{\text{SB}}/R_a = q^{-2/3}/2$ at the point of destruction, as seen in the figure.

This figure determines the parameter space that we must simulate to capture the diverse flow morphologies of the systems that undergo engulfment. In Section 4.1, we found that the drag coefficients are independent of R_{SB}/R_a in the gravitational regime. The blue region in Figure 8 shows this regime. Therefore, hydrodynamical simulations need to span only the transition and geometrical regimes. Each square in the Figure represents a hydrodynamical simulation, of which we ran 428.

5.2. Orbital decay trajectories

The equation of motion for the SB inside the star is

$$M_{\text{SB}} \frac{d\mathbf{v}}{dt} = (M_{\text{SB}} - \rho V_{\text{SB}}) \mathbf{g} + \mathbf{F}_{\text{drag}}, \quad (21)$$

where \mathbf{v} is the velocity of the SB, t is time, V_{SB} is the volume of the SB, and $\mathbf{g} = -GM_{\text{enc}}\hat{\mathbf{r}}/r^2$ is the gravitational acceleration from the mass enclosed by the SB's orbit. The term $\rho V_{\text{SB}}\hat{\mathbf{g}}$ is the buoyancy acting on the SB, which is important when the local density equals the average density of the SB. Since the local density is always smaller than the average enclosed density, and the SB will be tidally disrupted approximately when the average enclosed density is equal to its own mean density, buoyancy won't be important before SB destruction.

We integrate equation 21 numerically using the IAS15 (Rein & Spiegel 2015) integrator from the N-body code REBOUND (Rein & Liu 2012). At every timestep, we compute the dimensionless parameters ($q, \varepsilon_\rho, R_{\text{SB}}/R_a$) and linearly interpolate

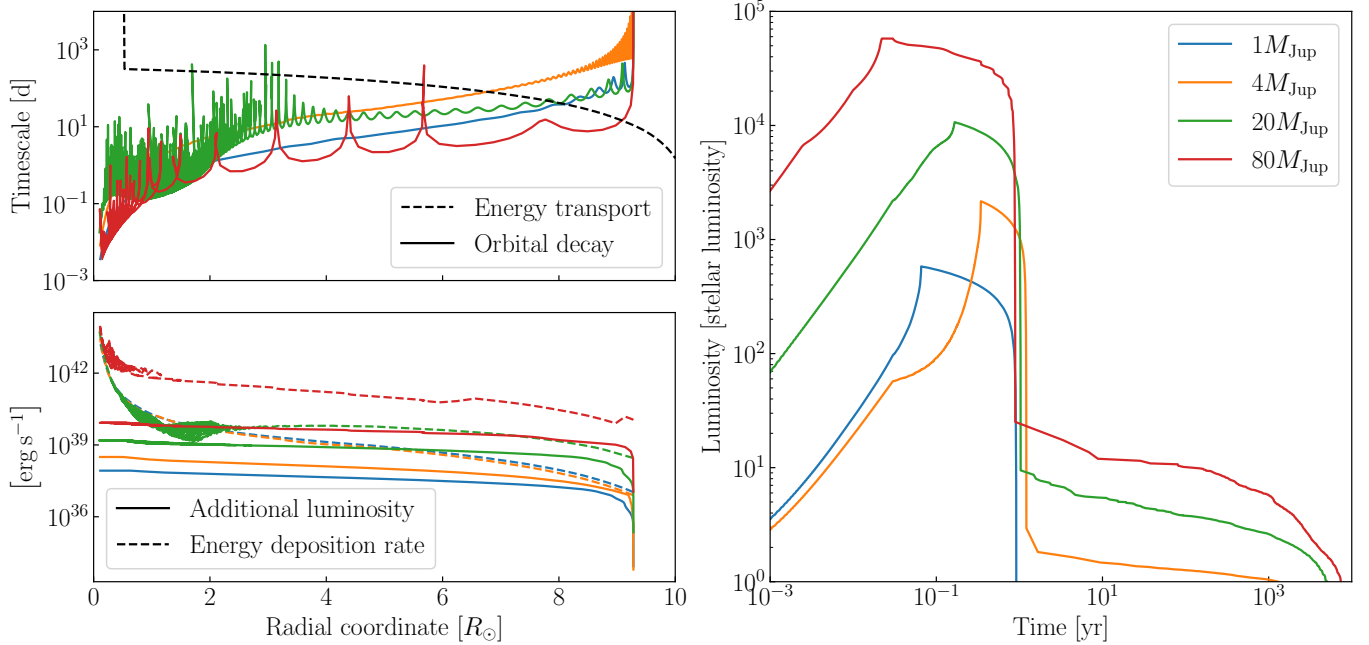


Figure 12. Top left panel: orbital decay and energy transport timescales as a function of the radial coordinate r of the substellar body (SB) inside the star. The orbital decay timescales for the two more massive substellar bodies show peaks because we define the orbital decay timescale as $|r/\dot{r}|$, and as a result of eccentricity in the orbit \dot{r} changes sign. Bottom left panel: rate of energy deposition and luminosity (excluding the stellar luminosity), again as a function of position inside the profile. When the energy transport timescale time is much longer than the orbital decay timescale, the luminosity is much smaller than the energy deposition rate. Right panel: luminosity as a function of time, in units of the unperturbed stellar luminosity.

the drag coefficients C_g and C_p we measured in the hydrodynamical simulations. For points outside the domain of the interpolation, we used the nearest available point.

We initially place the SB in a circular orbit at an orbital separation $0.9R_*$. At every timestep we interpolate the properties of the stellar profile using the GSL implementation of the Steffen method (Steffen 1990). We stop the integration when $r \leq R_{\text{SB}}$, and apply the destruction criteria during postprocessing.

We compute stellar profiles using MESA. The orbital decay timescale is $\lesssim 400$ yr for the systems we consider here (a $1M_{\text{Jup}}$ planet inside a $1M_{\odot}$ star at the tip of the RGB takes ≈ 400 yr). On the other hand, the timescales R/\dot{R} and L/\dot{L} over which radius and luminosity change significantly, respectively, are $\gtrsim 10^6$ yr throughout the RGB. Therefore, stellar structure doesn't change significantly as a result of stellar evolution over the timescales relevant to engulfment. We do not model the effects of engulfment on stellar structure, and use a single unperturbed MESA profile throughout our integration of the equation of motion of the SB.

Figure 10 and Figure 11 contrast the orbital decay trajectories obtained by using either analytical ($C_p = 0.25$, $C_g = 1$) or numerical drag coefficients, for two different systems. We chose systems whose orbital decay timescales were the smallest compared to the orbital period at their initial separations, so that their trajectories were easy to visualize. Figure 10 shows the trajectories for a Jupiter-like planet inside a $1M_{\odot}$ star evolved to $10R_{\odot}$. The orbit remains nearly circular, so

the energy deposition profiles are similar when using analytical or numerical drag coefficients. However, the orbit decays a factor ≈ 2 faster with the numerical coefficients. The timescale of energy transfer from the orbit into the star determines whether the star will transport the energy to the surface, or react dynamically. This distinction is particularly relevant for the stellar envelope, in which convection can carry energy to the surface quickly, lowering the efficiency of energy deposition (Wilson & Nordhaus 2019, 2020, 2022).

Figure 11 shows the trajectories for a $80M_{\text{Jup}}$ brown dwarf inside a star evolved to $100R_{\odot}$. For this system, both models for the drag coefficients yield similar orbital decay timescales, but the orbit is significantly more eccentric when using numerical drag coefficients. As discussed in Section 3, our hydrodynamical simulations neglect eccentricity, and therefore do not capture the flow morphology when the orbit of the SB is significantly eccentric. However, they show that at least small eccentricities arise from initially circular orbits faster than suggested by analytical drag. The evolution of the eccentricity is important for many types of systems. For the most massive SBs that can eject the envelope, it determines the eccentricity of their orbit around the stellar remnant (Szölgény et al. 2022). For small SBs, the eccentricity at the point of destruction determines the redistribution of their enriched material throughout the star.

5.3. Stellar brightening

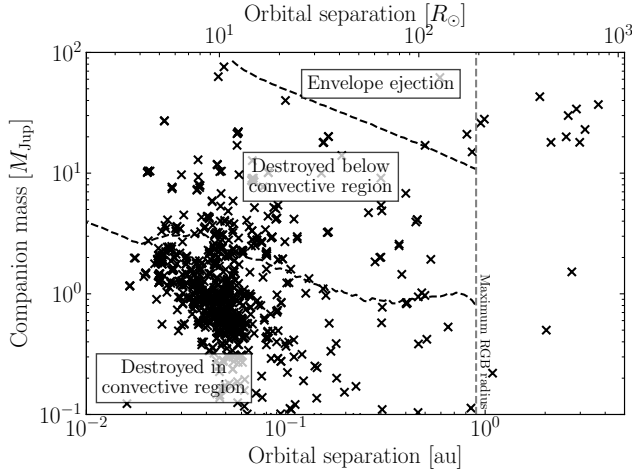


Figure 13. Engulfment outcomes for known substellar bodies (SBs, [NASA Exoplanet Archive 2022](#)), as a function of SB mass and orbital separation. This figure assumes that SBs are engulfed at their current separations and that they all orbit $1M_{\odot}$ stars. At a fixed SB mass, envelope ejection becomes easier as the star ascends the red giant branch because its binding energy decreases. A large fraction of SBs engulfed early in post-main-sequence evolution will dissolve in the convective region, yielding potential surface abundance enhancements of the ${}^7\text{Li}$ isotope. We also show systems with orbital separations larger than the maximum stellar radius during the RGB; if tidal forces lead to the engulfment of massive brown dwarfs with orbital separations larger than this maximum RGB radius (i.e., the brown dwarfs in the upper right region of the figure), they could eject the stellar envelope.

Planetary engulfment results in a transient dominated by recombination in mass ejected from the outer layers of the star ([Metzger et al. 2012](#)). Since we do not model changes to stellar structure, we study only the long-term emission resulting from the eventual transport of orbital energy from the deep layers of the star to its surface. If an energy dE is deposited into the star, the upper bound (assuming all energy leaves as radiation) for the average increase in stellar luminosity is $dL = dE/\tau_{\text{KH}}$, where τ_{KH} is the energy transport timescale from the location of energy deposition to the surface. More generally, for continuous energy deposition, the time-averaged additional luminosity at time t is

$$\Delta L(t) = \int_{t_0}^t \frac{\dot{E}}{\tau_{\text{KH}}} dt', \quad (22)$$

where we determine t_0 by noticing that energy deposited a time $t - t_0$ ago contributes to the increase in the average luminosity only if $t - t_0 \leq \tau_{\text{KH}}(t_0)$, since if $t - t_0 > \tau_{\text{KH}}(t_0)$, the energy deposited at t_0 has already been radiated away. If the energy deposition increases sharply in the inner regions of the star, $\dot{E} \approx \delta(t' - t) \Delta E(t')$ in equation 22, and $\Delta L \approx \Delta E/\tau_{\text{KH}}$ (e.g., [MacLeod et al. 2018](#)).

We compute \dot{E} from the work per unit time done by the drag forces,

$$\dot{E} = -\mathbf{F}_{\text{drag}} \cdot \mathbf{v}. \quad (23)$$

We compute the energy transport timescale by adding the cell crossing times in the stellar profile. The most effective energy transport mechanism at each cell (either radiative diffusion or convection) determines the crossing time for that cell.

Figure 12 shows the quantities involved in our calculation of the average luminosity for the engulfment of SBs of varying masses by a $1M_{\odot}$ star evolved to $10R_{\odot}$. The top left panel compares the orbital decay and energy transport timescales as a function of the orbital separation (equivalently, time). When the orbital decay timescale is much longer than the energy transport timescale, the luminosity is close to the energy deposition rate, whereas deep in the envelope the energy transport timescale is much longer than the orbital decay timescale, making the luminosity much smaller than the energy deposition rate. The bottom left panel shows this behavior. The right panel shows the luminosity.

From $R_{\star} = 10R_{\odot}$ to the tip of the RGB, the additional luminosity from engulfing SBs of most masses $\gtrsim M_{\text{Jup}}$ is comparable or larger than the stellar luminosity, in some cases by several orders of magnitude (see [Metzger et al. 2017](#)). SBs engulfed early in the post-main-sequence have higher energy deposition rates (because of the higher stellar density), and the stars that engulfed them are dimmer. On the other hand, evolved stars are sparser and more luminous, but have smaller energy transport timescales at the point of SB destruction. While these luminosity estimates rely on Equation 22 (which doesn't accurately describe radiative transfer inside the star) and depend on uncertain processes (such as the destruction of the SB), they suggest that engulfment is energetically significant throughout the post-main-sequence.

After SB destruction, the timescale for the luminosity to return to its original value is roughly the energy transport timescale at the point of destruction. The energy transport timescale at the point of destruction becomes shorter as the star ascends the RGB. For a given star, more massive SBs, which tend to also be denser as a result of the mass-radius relation, will result in a longer increase in luminosity because they survive deeper into the envelope. For a Sun-like star evolved to $10R_{\odot}$, the time it takes for the star to return to its original luminosity ranges from ~ 1 yr for a $1M_{\text{Jup}}$ planet to ~ 5000 yr for a $80M_{\text{Jup}}$ brown dwarf, as shown in Figure 12. On the other hand, for a model of the Sun at the tip of the RGB, the time ranges from ~ 1 yr to ~ 25 yr for the same range of SB masses.

5.4. Engulfment outcomes

Figure 13 shows known SBs ([NASA Exoplanet Archive 2022](#)) as a function of their mass and present-day orbital separation. The dashed line near the top-right corner shows the minimum SB mass for envelope ejection, assuming all deposited energy contributes to the ejection. Since the trajectories of some of the massive SBs that can eject the envelope are likely eccentric (Figure 11), we compute this line using

the analytical values for the drag coefficients. For destroyed SBs, the figure shows whether they’ll be destroyed in the convective zone or below it, according to the analytical destruction estimates of Equations 3 and 4. This figure assumes SBs are engulfed at their present-day orbital separations, and that all SBs orbit $1M_{\odot}$ stars (the average stellar mass reported for these SBs’ planetary systems is $1.12M_{\odot}$, with a standard deviation of $\sim 17\%$).

Under these assumptions, Figure 13 suggests massive SBs can eject the envelopes of evolved Sun-like stars through the transfer of orbital energy. This figure also shows that a substantial fraction of known SBs might be destroyed in the convective region of their host stars, particularly those at closer orbital separations because they are engulfed when the star is more compact and disrupts them more easily. The ${}^7\text{Li}$ contained in these SBs could be carried via convection to the surface, resulting in enhanced surface abundances. However, the mean molecular weight of the SB’s enriched material is much higher than that of its surroundings. Some of that material could settle in a layer near the base of the convective region and eventually reach the radiative core (Vauclair 2004; Jia & Spruit 2018). Intermediate-mass SBs (those in the central region of the plot) are massive enough to survive below the base of the convective region, perhaps resulting in opacity changes detectable through asteroseismology.

6. CONCLUSIONS

We studied the engulfment of substellar bodies (SBs) by evolved stars using hydrodynamical simulations of the flow in the vicinity of an engulfed SB (the “wind tunnel” framework, schematically depicted in Figure 5). The steps in our numerical framework are:

1. Determine the hydrodynamical parameter space for planetary engulfment. In particular, the range of values for the dimensionless parameters that affect the morphology of the flow around an engulfed SB.
2. Run hydrodynamical simulations that span this parameter space, characterize the resulting morphologies, and measure the drag coefficients for the drag forces acting on the SB.
3. Use the drag coefficients to integrate the equation of motion of an engulfed SB, and estimate observational signatures and outcomes of engulfment.

Some of our main findings are:

- The interactions of engulfed SBs with their environment are geometrical (ram pressure drag) and gravitational (gravitational drag). Geometrical interactions become increasingly important throughout engulfment (Figure 2, Figure 8). All SBs are in the geometrical regime when they are destroyed or when they eject the envelope (Figure 4).
- According to semi-analytical estimates, tidal disruption is the dominant destruction process for SBs with masses $\gtrsim 1M_{\text{Jup}}$ at most stages of stellar evolution.

- Many SBs will be in the gravitational regime at the onset of engulfment, and transition to the geometrical regime as their orbit shrinks. Our hydrodynamical simulations characterize this transition regime qualitatively (Figure 6) and quantitatively (Figure 7).

- The engulfment of an SB could increase the luminosity of a star by up to several orders of magnitude. The time it takes for the star to return to its original luminosity depends on its evolutionary stage and the mass of the SB (Section 5.3; Figure 12).

- Massive SBs could eject the stellar envelope via transfer of orbital energy, if the transferred energy can be efficiently distributed within the envelope (Figure 13). Small SBs are destroyed in the convective region.

We discussed the applicability of the wind tunnel framework to planetary engulfment in Section 3. As implemented in this work, the framework assumes that the density gradient in the stellar envelope and the velocity of the SB are perpendicular, and that the SB moves at approximately the circular Keplerian speed. These assumptions do not hold for some massive SBs, whose orbits develop significant eccentricities during engulfment. For this reason, we used analytical drag coefficients when computing the minimum mass required for envelope ejection. The evolution of the internal structure of the SB and the star remains a significant uncertainty in our calculations. We model the SB as a rigid body with a reflective boundary; while we approximately account for tidal and ram pressure disruption to determine the location in the star where the SB will be destroyed, only hydrodynamical models can describe these processes in detail. Future work could study the evolution of the SB’s internal structure to determine the conditions and timescales associated with its destruction. Simulations of the entire star can help understand its response to engulfment. Here we used a simplified model for energy transport to estimate the engulfment luminosity; more sophisticated stellar models including radiative transfer could constrain these observational signatures. The numerical framework we introduced here can be used to study the dynamics of planetary engulfment using comparatively inexpensive simulations that capture the physics of the flow at the scale of the SB.

We thank the anonymous referee for feedback that improved many aspects of this work. We thank Brant Robertson, Ruth Murray-Clay, and Yufeng Du for discussions, and Arcelia Hermosillo-Ruiz for discussions about REBOUND. We acknowledge use of the lux supercomputer at UC Santa Cruz, funded by NSF MRI grant AST 1828315, and thank Brant Robertson and Josh Sonstroem for help using lux. The FLASH code was in part developed by the DOE NNSA-ASC OASCR Flash Center at the University of Chicago. R.Y. is grateful for support from a Doctoral Fellowship from the University of California institute for Mexico and the United States (UCMEXUS) and the Consejo Nacional de Ciencia y Tecnología (CONACyT), a Texas Advanced Computing Center (TACC) Frontera Computational Science Fellowship, and a National Aeronautics and Space Administration (NASA) Future Investigators in NASA Earth and Space Science and Technology (FINESST) Fellowship (award 21-ASTRO21-0068). R.W.E. is supported by the National Science Foundation Graduate Research Fellowship Program (Award #1339067), the Heising-Simons Foundation, and the Vera Rubin Presidential Chair for Diversity at UCSC. A. M-B is supported by NASA through the NASA Hubble Fellowship grant HST-HF2-51487.001-A awarded by the Space Telescope Science Institute, which is operated by the Association of Universities for Research in Astronomy, Inc., for NASA, under contract NAS5-26555. E. R-R thanks the Heising-Simons Foundation and the NSF (AST-1911206, AST-1852393, and AST-1615881) for support. M.M. acknowledges support from the National Science Foundation under Grant No. 1909203. Any opinions, findings, and conclusions or recommendations expressed in this material are those of the authors and do not necessarily reflect the views of the NSF.

Software: FLASH 4.6.2 (Fryxell et al. 2000; Dubey et al. 2014, 2015), GNU Scientific Library 2.7 (Galassi et al. 2009), HDF5 (The HDF Group 1997-NNNN), matplotlib 3.6.2 (Hunter 2007), MESA (Buchler & Yueh 1976; Fuller et al. 1985; Iglesias & Rogers 1993; Oda et al. 1994; Saumon et al. 1995; Iglesias & Rogers 1996; Itoh et al. 1996; Langanke & Martínez-Pinedo 2000; Timmes & Swesty 2000; Rogers & Nayfonov 2002; Irwin 2004; Ferguson et al. 2005; Cassisi et al. 2007; Chugunov et al. 2007; Cyburt et al. 2010; Potekhin & Chabrier 2010; Paxton et al. 2011, 2013, 2015, 2018, 2019), MESA SDK (Townsend 2021), numpy 1.23.5 (Harris et al. 2020), py_mesa_reader (Wolf & Schwab 2017), scipy 1.9.3 (Virtanen et al. 2020), unyt 2.9.3 (Goldbaum et al. 2018), yt 4.1.2 (Turk et al. 2011).

APPENDIX

A. NUMERICAL TESTS

A.1. Wind tunnel

Figure 14 shows the ram pressure drag coefficient in a simulation with $\varepsilon_\rho = 1$ and $R_{\text{SB}}/R_a = 0.6$ at several reso-

lutions. We chose a value of R_{SB}/R_a for which computing the ram pressure drag would be the hardest numerically. If $R_{\text{SB}} > R_a$, the SB is a larger fraction of the domain size ($L_{\text{domain}} = 10 \max(R_{\text{SB}}, R_a)$), so it is easier to resolve. On the other hand, if $R_{\text{SB}} \ll R_a$, the pressure field around the SB

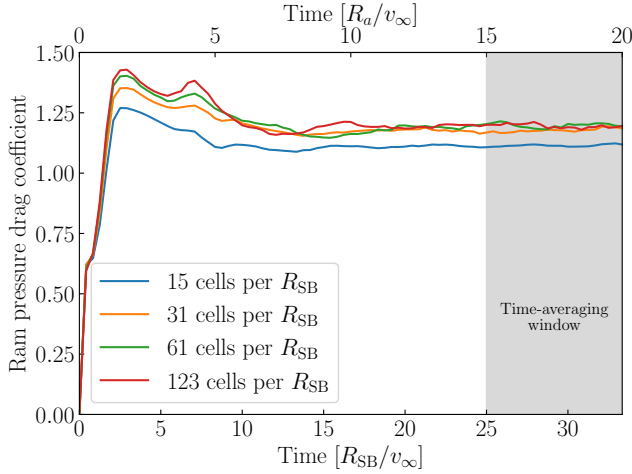


Figure 14. Ram pressure drag coefficient as a function of time, for a simulation with $R_{\text{SB}}/R_a = 0.6$ and $\varepsilon_\rho = 1$. Each line corresponds to a different resolution at the surface of the object. We compute the drag coefficient for a simulation by time-averaging the time-dependent drag coefficient between $15 \max(R_{\text{SB}}, R_a)/v_\infty$ and $20 \max(R_{\text{SB}}, R_a)/v_\infty$.

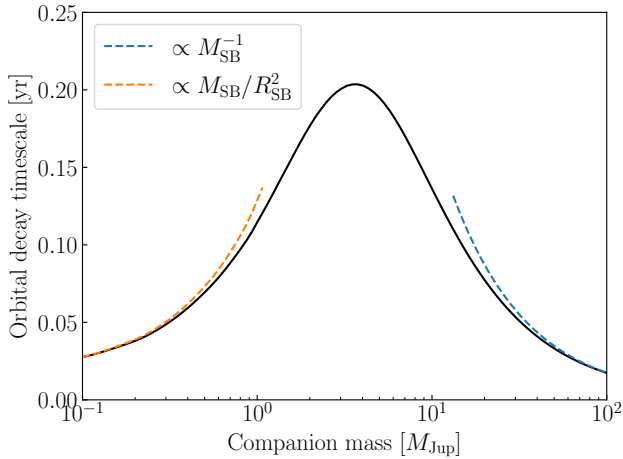


Figure 15. Orbital decay time for substellar bodies as a function of their mass, inside a model of a $1M_\odot$ star evolved to $10R_\odot$.

is spherically symmetric (Section 4). The hardest simulations in which to measure ram pressure drag are those with intermediate values of R_{SB}/R_a , for which R_{SB} is small compared to the length of the domain, but for which the pressure around the SB is still asymmetric. The maximum resolution in our test has 122 cells per R_{SB} . The ram pressure drag coefficient of a simulation with 31 cells per R_{SB} had a relative error (compared to the simulation with the highest resolution) of $\approx 1.5\%$. We set the refinement in all our simulations such that there are at least 31 cells per R_{SB} .

A.2. Equation of motion integration

We tested the implementation of the two effects we account for that deviate from the standard two-body problem: the

change of the mass enclosed by the orbit of the SB, and the drag forces.

We integrated the orbit of a $1M_{\text{Jup}}$ companion inside a star of radius $R_\star = 10R_\odot$ without drag forces. The initial radial coordinate of the SB is $9R_\odot$, and its initial speed is 70% of the circular Keplerian speed. After 10^4 dynamical times of the star, the specific orbital energy of the companion

$$E_{\text{orb,sp}} = \frac{v^2}{2} - \frac{GM_{\text{enc}}}{r} + G \int_{M_{\text{enc}}}^{M_\star} \frac{dM'_{\text{enc}}}{r} \quad (\text{A1})$$

was conserved to within a fractional error 5×10^{-7} .

We then integrated trajectories inside the same star for SBs of different masses, including drag forces (with drag coefficients $C_g = 1$ and $C_p = 0.25$). We initially place the SB in a circular Keplerian orbit at $9R_\odot$. For each SB mass, we computed the corresponding SB radius using the mass-radius relation, as discussed in Section 2. Figure 15 confirms that, for this star, in the low and high mass limits the orbital decay timescale scales as $M_{\text{SB}}/R_{\text{SB}}^2$ and M_{SB}^{-1} , respectively (see equations 7 and 8). The work done by drag forces was equal to the change in orbital energy to within a fractional error 2×10^{-6} .

B. FITTING FORMULÆ

We fit the results of Figure 13. The minimum companion mass required to eject the envelope of a $1M_\odot$ star as a function of its radius is

$$\frac{M_{\text{SB}}}{M_{\text{Jup}}} = \frac{1.3589x^2 + 2.1182x - 196.53}{5.0709 \times 10^{-4}x^3 + 0.032124x^2 - 0.51638x + 1}, \quad (\text{B2})$$

where $x \equiv R_\star/R_\odot$. This formula is valid when $11.45 \leq R_\star/R_\odot \leq 193.7$ and agrees with the Figure to within 1.1%.

The minimum mass for a companion to survive below the base of the convective zone is

$$\frac{M_{\text{SB}}}{M_{\text{Jup}}} = (b_3x^3 + b_2x^2 + b_1x + 1)^{-1} \sum_{i=0}^5 a_i x^i, \quad (\text{B3})$$

where $x \equiv \log_{10}(R_\star/R_\odot)$, $b_1 = -3.01905$, $b_2 = 2.89041$, $b_3 = -0.767818$, and

$$a_i = \{5.7773, -23.548, 36.3736, -26.1053, 8.96339, -1.20016\}. \quad (\text{B4})$$

This formula is valid when $2 \leq R_\star/R_\odot \leq 193.7$ and agrees with the Figure to within 7.9%.

C. DATA AND SOFTWARE AVAILABILITY

The software and data required to reproduce our results are available under the digital object identifiers [10.5281/zenodo.6368227](https://doi.org/10.5281/zenodo.6368227) and [10.5281/zenodo.6371752](https://doi.org/10.5281/zenodo.6371752), respectively. These repositories include the wind tunnel FLASH setup, the code we used to integrate the equation of motion of the engulfed companion, and the drag coefficients we measured in our hydrodynamical simulations.

REFERENCES

- Adamów, M., Niedzielski, A., Villaver, E., et al. 2015, *A&A*, 581, A94, doi: [10.1051/0004-6361/201526582](https://doi.org/10.1051/0004-6361/201526582)
- Adamów, M., Niedzielski, A., Villaver, E., Wolszczan, A., & Nowak, G. 2014, *A&A*, 569, A55, doi: [10.1051/0004-6361/201423400](https://doi.org/10.1051/0004-6361/201423400)
- Aguilera-Gómez, C., Chanamé, J., Pinsonneault, M. H., & Carlberg, J. K. 2016a, *ApJL*, 833, L24, doi: [10.3847/2041-8213/833/2/L24](https://doi.org/10.3847/2041-8213/833/2/L24)
- . 2016b, *ApJ*, 829, 127, doi: [10.3847/0004-637X/829/2/127](https://doi.org/10.3847/0004-637X/829/2/127)
- Almeida, L. A., Damineli, A., Rodrigues, C. V., Pereira, M. G., & Jablonski, F. 2017, *MNRAS*, 472, 3093, doi: [10.1093/mnras/stx2150](https://doi.org/10.1093/mnras/stx2150)
- Balachandran, S. C., Fekel, F. C., Henry, G. W., & Uitenbroek, H. 2000, *ApJ*, 542, 978, doi: [10.1086/317055](https://doi.org/10.1086/317055)
- Baumann, P., Ramírez, I., Meléndez, J., Asplund, M., & Lind, K. 2010, *A&A*, 519, A87, doi: [10.1051/0004-6361/201015137](https://doi.org/10.1051/0004-6361/201015137)
- Beuermann, K., Dreizler, S., Hessman, F. V., et al. 2013, *A&A*, 558, A96, doi: [10.1051/0004-6361/201322241](https://doi.org/10.1051/0004-6361/201322241)
- Bodenheimer, P. 1965, *ApJ*, 142, 451, doi: [10.1086/148310](https://doi.org/10.1086/148310)
- Bondi, H. 1952, *MNRAS*, 112, 195, doi: [10.1093/mnras/112.2.195](https://doi.org/10.1093/mnras/112.2.195)
- Bondi, H., & Hoyle, F. 1944, *MNRAS*, 104, 273, doi: [10.1093/mnras/104.5.273](https://doi.org/10.1093/mnras/104.5.273)
- Breedt, E., Gänsicke, B. T., Girven, J., et al. 2012, *MNRAS*, 423, 1437, doi: [10.1111/j.1365-2966.2012.20965.x](https://doi.org/10.1111/j.1365-2966.2012.20965.x)
- Brown, J. A., Sneden, C., Lambert, D. L., & Dutchover, Edward, J. 1989, *ApJS*, 71, 293, doi: [10.1086/191375](https://doi.org/10.1086/191375)
- Buchler, J. R., & Yueh, W. R. 1976, *ApJ*, 210, 440, doi: [10.1086/154847](https://doi.org/10.1086/154847)
- Cameron, A. G. W., & Fowler, W. A. 1971, *ApJ*, 164, 111, doi: [10.1086/150821](https://doi.org/10.1086/150821)
- Carlberg, J. K., Smith, V. V., Cunha, K., Majewski, S. R., & Rood, R. T. 2010, *ApJL*, 723, L103, doi: [10.1088/2041-8205/723/1/L103](https://doi.org/10.1088/2041-8205/723/1/L103)
- Carlos, M., Nissen, P. E., & Meléndez, J. 2016, *A&A*, 587, A100, doi: [10.1051/0004-6361/201527478](https://doi.org/10.1051/0004-6361/201527478)
- Carlos, M., Meléndez, J., Spina, L., et al. 2019, *MNRAS*, 485, 4052, doi: [10.1093/mnras/stz681](https://doi.org/10.1093/mnras/stz681)
- Casewell, S. L., Burleigh, M. R., Wynn, G. A., et al. 2012, *ApJL*, 759, L34, doi: [10.1088/2041-8205/759/2/L34](https://doi.org/10.1088/2041-8205/759/2/L34)
- Casewell, S. L., Belardi, C., Parsons, S. G., et al. 2020, *MNRAS*, 497, 3571, doi: [10.1093/mnras/staa1608](https://doi.org/10.1093/mnras/staa1608)
- Cassisi, S., Potekhin, A. Y., Pietrinferni, A., Catelan, M., & Salaris, M. 2007, *ApJ*, 661, 1094, doi: [10.1086/516819](https://doi.org/10.1086/516819)
- Chabrier, G., Baraffe, I., Leconte, J., Gallardo, J., & Barman, T. 2009, in *American Institute of Physics Conference Series*, Vol. 1094, 15th Cambridge Workshop on Cool Stars, Stellar Systems, and the Sun, ed. E. Stempels, 102–111, doi: [10.1063/1.3099078](https://doi.org/10.1063/1.3099078)
- Charbonnel, C., & Balachandran, S. C. 2000, *A&A*, 359, 563, <https://arxiv.org/abs/astro-ph/0005280>
- Charbonnel, C., & Lagarde, N. 2010, *A&A*, 522, A10, doi: [10.1051/0004-6361/201014432](https://doi.org/10.1051/0004-6361/201014432)
- Charpinet, S., Fontaine, G., Brassard, P., et al. 2011, *Nature*, 480, 496, doi: [10.1038/nature10631](https://doi.org/10.1038/nature10631)
- Chugunov, A. I., Dewitt, H. E., & Yakovlev, D. G. 2007, *PhRvD*, 76, 025028, doi: [10.1103/PhysRevD.76.025028](https://doi.org/10.1103/PhysRevD.76.025028)
- Cyburt, R. H., Amthor, A. M., Ferguson, R., et al. 2010, *ApJS*, 189, 240, doi: [10.1088/0067-0049/189/1/240](https://doi.org/10.1088/0067-0049/189/1/240)
- Darwin, G. H. 1879, *Proceedings of the Royal Society of London Series I*, 29, 168
- De, S., MacLeod, M., Everson, R. W., et al. 2020, *ApJ*, 897, 130, doi: [10.3847/1538-4357/ab9ac6](https://doi.org/10.3847/1538-4357/ab9ac6)
- Deepak, & Reddy, B. E. 2019, *MNRAS*, 484, 2000, doi: [10.1093/mnras/stz128](https://doi.org/10.1093/mnras/stz128)
- Deliyannis, C. P., Cunha, K., King, J. R., & Boesgaard, A. M. 2000, *AJ*, 119, 2437, doi: [10.1086/301327](https://doi.org/10.1086/301327)
- Dubey, A., Antypas, K., Calder, A. C., et al. 2014, *International Journal of High Performance Computing Applications*, 28, 225, doi: <http://dx.doi.org/10.1177/1094342013505656>
- Dubey, A., Weide, K., Lee, D., et al. 2015, *Software: Practice and Experience*, 45, 233
- Everson, R. W., MacLeod, M., De, S., Macias, P., & Ramirez-Ruiz, E. 2020, *ApJ*, 899, 77, doi: [10.3847/1538-4357/aba75c](https://doi.org/10.3847/1538-4357/aba75c)
- Fabrycky, D., & Tremaine, S. 2007, *ApJ*, 669, 1298, doi: [10.1086/521702](https://doi.org/10.1086/521702)
- Ferguson, J. W., Alexander, D. R., Allard, F., et al. 2005, *ApJ*, 623, 585, doi: [10.1086/428642](https://doi.org/10.1086/428642)
- Fortney, J. J., Marley, M. S., & Barnes, J. W. 2007, *ApJ*, 659, 1661, doi: [10.1086/512120](https://doi.org/10.1086/512120)
- Fragos, T., Andrews, J. J., Ramirez-Ruiz, E., et al. 2019, *ApJL*, 883, L45, doi: [10.3847/2041-8213/ab40d1](https://doi.org/10.3847/2041-8213/ab40d1)
- Fryxell, B., Olson, K., Ricker, P., et al. 2000, *ApJS*, 131, 273, doi: [10.1086/317361](https://doi.org/10.1086/317361)
- Fuller, G. M., Fowler, W. A., & Newman, M. J. 1985, *ApJ*, 293, 1, doi: [10.1086/163208](https://doi.org/10.1086/163208)
- Galassi, M., et al. 2009, *GNU Scientific Library Reference Manual*, 3rd edn.
- Gallet, F., Bolmont, E., Mathis, S., Charbonnel, C., & Amard, L. 2017, *A&A*, 604, A112, doi: [10.1051/0004-6361/201730661](https://doi.org/10.1051/0004-6361/201730661)
- Gao, Q., Shi, J.-R., Yan, H.-L., et al. 2019, *ApJS*, 245, 33, doi: [10.3847/1538-4365/ab505c](https://doi.org/10.3847/1538-4365/ab505c)
- Geier, S., Edelmann, H., Heber, U., & Morales-Rueda, L. 2009, *ApJL*, 702, L96, doi: [10.1088/0004-637X/702/1/L96](https://doi.org/10.1088/0004-637X/702/1/L96)
- Goldbaum, N. J., ZuHone, J. A., Turk, M. J., Kowalik, K., & Rosen, A. L. 2018, *Journal of Open Source Software*, 3, 809, doi: [10.21105/joss.00809](https://doi.org/10.21105/joss.00809)
- Grunblatt, S. K., Saunders, N., Sun, M., et al. 2022, *arXiv e-prints*, arXiv:2201.04140. <https://arxiv.org/abs/2201.04140>

- Gruzinov, A., Levin, Y., & Matzner, C. D. 2020, *MNRAS*, 492, 2755, doi: [10.1093/mnras/staa013](https://doi.org/10.1093/mnras/staa013)
- Guidarelli, G., Nordhaus, J., Chamandy, L., et al. 2019, *MNRAS*, 490, 1179, doi: [10.1093/mnras/stz2641](https://doi.org/10.1093/mnras/stz2641)
- Harris, C. R., Millman, K. J., van der Walt, S. J., et al. 2020, *Nature*, 585, 357–362, doi: [10.1038/s41586-020-2649-2](https://doi.org/10.1038/s41586-020-2649-2)
- Hoyle, F., & Lyttleton, R. A. 1939, *Proceedings of the Cambridge Philosophical Society*, 35, 405, doi: [10.1017/S0305004100021150](https://doi.org/10.1017/S0305004100021150)
- Hunter, J. D. 2007, *Computing in Science & Engineering*, 9, 90, doi: [10.1109/MCSE.2007.55](https://doi.org/10.1109/MCSE.2007.55)
- Iglesias, C. A., & Rogers, F. J. 1993, *ApJ*, 412, 752, doi: [10.1086/172958](https://doi.org/10.1086/172958)
- . 1996, *ApJ*, 464, 943, doi: [10.1086/177381](https://doi.org/10.1086/177381)
- Irwin, A. W. 2004, *The FreeEOS Code for Calculating the Equation of State for Stellar Interiors*. <http://freeeos.sourceforge.net/>
- Itoh, N., Hayashi, H., Nishikawa, A., & Kohyama, Y. 1996, *ApJS*, 102, 411, doi: [10.1086/192264](https://doi.org/10.1086/192264)
- Jia, S., & Spruit, H. C. 2018, *ApJ*, 864, 169, doi: [10.3847/1538-4357/aad77c](https://doi.org/10.3847/1538-4357/aad77c)
- Kaaz, N., Murguía-Berthier, A., Chatterjee, K., Liska, M., & Tekehovskoy, A. 2022, arXiv e-prints, arXiv:2201.11753. <https://arxiv.org/abs/2201.11753>
- Katz, B., Dong, S., & Malhotra, R. 2011, *PhRvL*, 107, 181101, doi: [10.1103/PhysRevLett.107.181101](https://doi.org/10.1103/PhysRevLett.107.181101)
- Kozai, Y. 1962, *AJ*, 67, 591, doi: [10.1086/108790](https://doi.org/10.1086/108790)
- Kruckow, M. U., Neunteufel, P. G., Di Stefano, R., Gao, Y., & Kobayashi, C. 2021, arXiv e-prints, arXiv:2107.05221. <https://arxiv.org/abs/2107.05221>
- Kumar, Y. B., Reddy, B. E., & Lambert, D. L. 2011, *ApJL*, 730, L12, doi: [10.1088/2041-8205/730/1/L12](https://doi.org/10.1088/2041-8205/730/1/L12)
- Lagos, F., Schreiber, M. R., Zorotovic, M., et al. 2021, *MNRAS*, 501, 676, doi: [10.1093/mnras/staa3703](https://doi.org/10.1093/mnras/staa3703)
- Langanke, K., & Martínez-Pinedo, G. 2000, *NuPhA*, 673, 481, doi: [10.1016/S0375-9474\(00\)00131-7](https://doi.org/10.1016/S0375-9474(00)00131-7)
- Lee, D. 2013, *Journal of Computational Physics*, 243, 269, doi: <https://doi.org/10.1016/j.jcp.2013.02.049>
- Li, H., Aoki, W., Matsuno, T., et al. 2018, *ApJL*, 852, L31, doi: [10.3847/2041-8213/aaa438](https://doi.org/10.3847/2041-8213/aaa438)
- Li, X., Chang, P., Levin, Y., Matzner, C. D., & Armitage, P. J. 2020, *MNRAS*, 494, 2327, doi: [10.1093/mnras/staa900](https://doi.org/10.1093/mnras/staa900)
- Littlefair, S. P., Dhillon, V. S., Marsh, T. R., et al. 2007, *MNRAS*, 381, 827, doi: [10.1111/j.1365-2966.2007.12285.x](https://doi.org/10.1111/j.1365-2966.2007.12285.x)
- . 2008, *MNRAS*, 388, 1582, doi: [10.1111/j.1365-2966.2008.13539.x](https://doi.org/10.1111/j.1365-2966.2008.13539.x)
- . 2006, *Science*, 314, 1578, doi: [10.1126/science.1133333](https://doi.org/10.1126/science.1133333)
- Liu, C., Li, L., Zhang, F., et al. 2012, *MNRAS*, 424, 1841, doi: [10.1111/j.1365-2966.2012.21285.x](https://doi.org/10.1111/j.1365-2966.2012.21285.x)
- Livio, M., & Soker, N. 1984, *MNRAS*, 208, 763, doi: [10.1093/mnras/208.4.763](https://doi.org/10.1093/mnras/208.4.763)
- MacLeod, M., Antoni, A., Murguía-Berthier, A., Macias, P., & Ramirez-Ruiz, E. 2017, *ApJ*, 838, 56, doi: [10.3847/1538-4357/aa6117](https://doi.org/10.3847/1538-4357/aa6117)
- MacLeod, M., Cantiello, M., & Soares-Furtado, M. 2018, *ApJL*, 853, L1, doi: [10.3847/2041-8213/aaa5fa](https://doi.org/10.3847/2041-8213/aaa5fa)
- MacLeod, M., & Ramirez-Ruiz, E. 2015a, *ApJ*, 803, 41, doi: [10.1088/0004-637X/803/1/41](https://doi.org/10.1088/0004-637X/803/1/41)
- . 2015b, *ApJL*, 798, L19, doi: [10.1088/2041-8205/798/1/L19](https://doi.org/10.1088/2041-8205/798/1/L19)
- Mallik, A., Reddy, B. E., & Muthumariappan, C. 2022, arXiv e-prints, arXiv:2201.09643. <https://arxiv.org/abs/2201.09643>
- Martell, S. L., & Shetrone, M. D. 2013, *MNRAS*, 430, 611, doi: [10.1093/mnras/sts661](https://doi.org/10.1093/mnras/sts661)
- Masset, F. S. 2017, *MNRAS*, 472, 4204, doi: [10.1093/mnras/stx2271](https://doi.org/10.1093/mnras/stx2271)
- Masset, F. S., & Velasco Romero, D. A. 2017, *MNRAS*, 465, 3175, doi: [10.1093/mnras/stw3008](https://doi.org/10.1093/mnras/stw3008)
- Maxted, P. F. L., Napiwotzki, R., Dobbie, P. D., & Burleigh, M. R. 2006, *Nature*, 442, 543, doi: [10.1038/nature04987](https://doi.org/10.1038/nature04987)
- McAllister, M. J., Littlefair, S. P., Baraffe, I., et al. 2015, *MNRAS*, 451, 114, doi: [10.1093/mnras/stv956](https://doi.org/10.1093/mnras/stv956)
- Meléndez, J., Schirbel, L., Monroe, T. R., et al. 2014, *A&A*, 567, L3, doi: [10.1051/0004-6361/201424172](https://doi.org/10.1051/0004-6361/201424172)
- Merlov, A., Bear, E., & Soker, N. 2021, *ApJL*, 915, L34, doi: [10.3847/2041-8213/ac0f7d](https://doi.org/10.3847/2041-8213/ac0f7d)
- Metzger, B. D., Giannios, D., & Spiegel, D. S. 2012, *MNRAS*, 425, 2778, doi: [10.1111/j.1365-2966.2012.21444.x](https://doi.org/10.1111/j.1365-2966.2012.21444.x)
- Metzger, B. D., Shen, K. J., & Stone, N. 2017, *MNRAS*, 468, 4399, doi: [10.1093/mnras/stx823](https://doi.org/10.1093/mnras/stx823)
- Monroe, T. R., Meléndez, J., Ramírez, I., et al. 2013, *ApJL*, 774, L32, doi: [10.1088/2041-8205/774/2/L32](https://doi.org/10.1088/2041-8205/774/2/L32)
- Muñoz, D. J., & Petrovich, C. 2020, *ApJL*, 904, L3, doi: [10.3847/2041-8213/abc564](https://doi.org/10.3847/2041-8213/abc564)
- Murguía-Berthier, A., MacLeod, M., Ramirez-Ruiz, E., Antoni, A., & Macias, P. 2017, *ApJ*, 845, 173, doi: [10.3847/1538-4357/aa8140](https://doi.org/10.3847/1538-4357/aa8140)
- Mustill, A. J., & Villaver, E. 2012, *ApJ*, 761, 121, doi: [10.1088/0004-637X/761/2/121](https://doi.org/10.1088/0004-637X/761/2/121)
- Naoz, S., Farr, W. M., & Rasio, F. A. 2012, *ApJL*, 754, L36, doi: [10.1088/2041-8205/754/2/L36](https://doi.org/10.1088/2041-8205/754/2/L36)
- NASA Exoplanet Archive. 2022, *Planetary Systems Composite Parameters*, Version: YYYY-MM-DD HH:MM, NExSci-Caltech/IPAC, doi: [10.26133/NEA13](https://doi.org/10.26133/NEA13)
- Nelemans, G., & Tauris, T. M. 1998, *A&A*, 335, L85. <https://arxiv.org/abs/astro-ph/9806011>
- Nordhaus, J., & Spiegel, D. S. 2013, *MNRAS*, 432, 500, doi: [10.1093/mnras/stt569](https://doi.org/10.1093/mnras/stt569)
- Nordhaus, J., Wellons, S., Spiegel, D. S., Metzger, B. D., & Blackman, E. G. 2011, *Proceedings of the National Academy of Sciences*, 108, 3135, doi: [10.1073/pnas.1015005108](https://doi.org/10.1073/pnas.1015005108)

- O'Connor, C. E., Liu, B., & Lai, D. 2021, *MNRAS*, 501, 507, doi: [10.1093/mnras/staa3723](https://doi.org/10.1093/mnras/staa3723)
- Oda, T., Hino, M., Muto, K., Takahara, M., & Sato, K. 1994, *Atomic Data and Nuclear Data Tables*, 56, 231, doi: [10.1006/adnd.1994.1007](https://doi.org/10.1006/adnd.1994.1007)
- Paczynski, B. 1976, in *Structure and Evolution of Close Binary Systems*, ed. P. Eggleton, S. Mitton, & J. Whelan, Vol. 73, 75
- Pala, A. F., Schmidtobreick, L., Tappert, C., Gänsicke, B. T., & Mehner, A. 2018, *MNRAS*, 481, 2523, doi: [10.1093/mnras/sty2434](https://doi.org/10.1093/mnras/sty2434)
- Parsons, S. G., Hermes, J. J., Marsh, T. R., et al. 2017, *MNRAS*, 471, 976, doi: [10.1093/mnras/stx1610](https://doi.org/10.1093/mnras/stx1610)
- Passy, J.-C., Mac Low, M.-M., & De Marco, O. 2012, *ApJL*, 759, L30, doi: [10.1088/2041-8205/759/2/L30](https://doi.org/10.1088/2041-8205/759/2/L30)
- Paxton, B., Bildsten, L., Dotter, A., et al. 2011, *ApJS*, 192, 3, doi: [10.1088/0067-0049/192/1/3](https://doi.org/10.1088/0067-0049/192/1/3)
- Paxton, B., Cantiello, M., Arras, P., et al. 2013, *ApJS*, 208, 4, doi: [10.1088/0067-0049/208/1/4](https://doi.org/10.1088/0067-0049/208/1/4)
- Paxton, B., Marchant, P., Schwab, J., et al. 2015, *ApJS*, 220, 15, doi: [10.1088/0067-0049/220/1/15](https://doi.org/10.1088/0067-0049/220/1/15)
- Paxton, B., Schwab, J., Bauer, E. B., et al. 2018, *ApJS*, 234, 34, doi: [10.3847/1538-4365/aaa5a8](https://doi.org/10.3847/1538-4365/aaa5a8)
- Paxton, B., Smolec, R., Schwab, J., et al. 2019, *ApJS*, 243, 10, doi: [10.3847/1538-4365/ab2241](https://doi.org/10.3847/1538-4365/ab2241)
- Peterson, R. C., Tarbell, T. D., & Carney, B. W. 1983, *ApJ*, 265, 972, doi: [10.1086/160739](https://doi.org/10.1086/160739)
- Piau, L., & Turck-Chièze, S. 2002, *ApJ*, 566, 419, doi: [10.1086/324277](https://doi.org/10.1086/324277)
- Potekhin, A. Y., & Chabrier, G. 2010, *Contributions to Plasma Physics*, 50, 82, doi: [10.1002/ctpp.201010017](https://doi.org/10.1002/ctpp.201010017)
- Privitera, G., Meynet, G., Eggenberger, P., et al. 2016a, *A&A*, 593, A128, doi: [10.1051/0004-6361/201628758](https://doi.org/10.1051/0004-6361/201628758)
- . 2016b, *A&A*, 591, A45, doi: [10.1051/0004-6361/201528044](https://doi.org/10.1051/0004-6361/201528044)
- Prša, A., Harmanec, P., Torres, G., et al. 2016, *AJ*, 152, 41, doi: [10.3847/0004-6256/152/2/41](https://doi.org/10.3847/0004-6256/152/2/41)
- Qureshi, A., Naoz, S., & Shkolnik, E. L. 2018, *ApJ*, 864, 65, doi: [10.3847/1538-4357/aad562](https://doi.org/10.3847/1538-4357/aad562)
- Rebassa-Mansergas, A., Zorotovic, M., Schreiber, M. R., et al. 2012, *MNRAS*, 423, 320, doi: [10.1111/j.1365-2966.2012.20880.x](https://doi.org/10.1111/j.1365-2966.2012.20880.x)
- Reddy, B. E., & Lambert, D. L. 2005, *AJ*, 129, 2831, doi: [10.1086/430190](https://doi.org/10.1086/430190)
- Rein, H., & Liu, S. F. 2012, *A&A*, 537, A128, doi: [10.1051/0004-6361/201118085](https://doi.org/10.1051/0004-6361/201118085)
- Rein, H., & Spiegel, D. S. 2015, *MNRAS*, 446, 1424, doi: [10.1093/mnras/stu2164](https://doi.org/10.1093/mnras/stu2164)
- Rogers, F. J., & Nayfonov, A. 2002, *ApJ*, 576, 1064, doi: [10.1086/341894](https://doi.org/10.1086/341894)
- Ruffert, M., & Arnett, D. 1994, *ApJ*, 427, 351, doi: [10.1086/174145](https://doi.org/10.1086/174145)
- Sandquist, E., Taam, R. E., Lin, D. N. C., & Burkert, A. 1998, *ApJL*, 506, L65, doi: [10.1086/311633](https://doi.org/10.1086/311633)
- Sandquist, E. L., Dokter, J. J., Lin, D. N. C., & Mardling, R. A. 2002, *ApJ*, 572, 1012, doi: [10.1086/340452](https://doi.org/10.1086/340452)
- Saumon, D., Chabrier, G., & van Horn, H. M. 1995, *ApJS*, 99, 713, doi: [10.1086/192204](https://doi.org/10.1086/192204)
- Schaffenroth, V., Barlow, B. N., Drechsel, H., & Dunlap, B. H. 2015, *A&A*, 576, A123, doi: [10.1051/0004-6361/201525701](https://doi.org/10.1051/0004-6361/201525701)
- Schaffenroth, V., Casewell, S. L., Schneider, D., et al. 2021, *MNRAS*, 501, 3847, doi: [10.1093/mnras/staa3661](https://doi.org/10.1093/mnras/staa3661)
- Schlaufman, K. C., & Winn, J. N. 2013, *ApJ*, 772, 143, doi: [10.1088/0004-637X/772/2/143](https://doi.org/10.1088/0004-637X/772/2/143)
- Schmidt, G. D., Szkody, P., Silvestri, N. M., et al. 2005, *ApJL*, 630, L173, doi: [10.1086/491702](https://doi.org/10.1086/491702)
- Shappee, B. J., & Thompson, T. A. 2013, *ApJ*, 766, 64, doi: [10.1088/0004-637X/766/1/64](https://doi.org/10.1088/0004-637X/766/1/64)
- Siess, L., & Livio, M. 1999, *MNRAS*, 308, 1133, doi: [10.1046/j.1365-8711.1999.02784.x](https://doi.org/10.1046/j.1365-8711.1999.02784.x)
- Silvestri, N. M., Lemagie, M. P., Hawley, S. L., et al. 2007, *AJ*, 134, 741, doi: [10.1086/519242](https://doi.org/10.1086/519242)
- Singh, R., Reddy, B. E., Bharat Kumar, Y., & Antia, H. M. 2019, *ApJL*, 878, L21, doi: [10.3847/2041-8213/ab2599](https://doi.org/10.3847/2041-8213/ab2599)
- Soares-Furtado, M., Cantiello, M., MacLeod, M., & Ness, M. K. 2021, *AJ*, 162, 273, doi: [10.3847/1538-3881/ac273c](https://doi.org/10.3847/1538-3881/ac273c)
- Socrates, A., Katz, B., Dong, S., & Tremaine, S. 2012, *ApJ*, 750, 106, doi: [10.1088/0004-637X/750/2/106](https://doi.org/10.1088/0004-637X/750/2/106)
- Soker, N. 1998, *AJ*, 116, 1308, doi: [10.1086/300503](https://doi.org/10.1086/300503)
- Staff, J. E., De Marco, O., Wood, P., Galaviz, P., & Passy, J.-C. 2016, *MNRAS*, 458, 832, doi: [10.1093/mnras/stw331](https://doi.org/10.1093/mnras/stw331)
- Steele, P. R., Saglia, R. P., Burleigh, M. R., et al. 2013, *MNRAS*, 429, 3492, doi: [10.1093/mnras/sts620](https://doi.org/10.1093/mnras/sts620)
- Steffen, M. 1990, *A&A*, 239, 443
- Stephan, A. P., Naoz, S., Gaudi, B. S., & Salas, J. M. 2020, *ApJ*, 889, 45, doi: [10.3847/1538-4357/ab5b00](https://doi.org/10.3847/1538-4357/ab5b00)
- Sun, M., Arras, P., Weinberg, N. N., Troup, N. W., & Majewski, S. R. 2018, *MNRAS*, 481, 4077, doi: [10.1093/mnras/sty2464](https://doi.org/10.1093/mnras/sty2464)
- Szölgvény, Á., MacLeod, M., & Loeb, A. 2022, *MNRAS*, 513, 5465, doi: [10.1093/mnras/stac1294](https://doi.org/10.1093/mnras/stac1294)
- The HDF Group. 1997-NNNN, Hierarchical Data Format, version 5
- Thun, D., Kuiper, R., Schmidt, F., & Kley, W. 2016, *A&A*, 589, A10, doi: [10.1051/0004-6361/201527629](https://doi.org/10.1051/0004-6361/201527629)
- Tiesinga, E., Mohr, P. J., Newell, D. B., & Taylor, B. N. 2021, *Rev. Mod. Phys.*, 93, 025010, doi: [10.1103/RevModPhys.93.025010](https://doi.org/10.1103/RevModPhys.93.025010)
- Timmes, F. X., & Swesty, F. D. 2000, *ApJS*, 126, 501, doi: [10.1086/313304](https://doi.org/10.1086/313304)
- Townsend, R. 2021, MESA SDK for Linux, 21.4.1, Zenodo, doi: [10.5281/zenodo.5802444](https://doi.org/10.5281/zenodo.5802444)
- Turk, M. J., Smith, B. D., Oishi, J. S., et al. 2011, *ApJS*, 192, 9, doi: [10.1088/0067-0049/192/1/9](https://doi.org/10.1088/0067-0049/192/1/9)
- van den Heuvel, E. P. J. 1976, in *Structure and Evolution of Close Binary Systems*, ed. P. Eggleton, S. Mitton, & J. Whelan, Vol. 73, 35

- van Roestel, J., Kupfer, T., Bell, K. J., et al. 2021, *ApJL*, 919, L26, doi: [10.3847/2041-8213/ac22b7](https://doi.org/10.3847/2041-8213/ac22b7)
- Vanderburg, A., Rappaport, S. A., Xu, S., et al. 2020, *Nature*, 585, 363, doi: [10.1038/s41586-020-2713-y](https://doi.org/10.1038/s41586-020-2713-y)
- Vauclair, S. 2004, *ApJ*, 605, 874, doi: [10.1086/382668](https://doi.org/10.1086/382668)
- Villaver, E., & Livio, M. 2009, *ApJL*, 705, L81, doi: [10.1088/0004-637X/705/1/L81](https://doi.org/10.1088/0004-637X/705/1/L81)
- Villaver, E., Livio, M., Mustill, A. J., & Siess, L. 2014, *ApJ*, 794, 3, doi: [10.1088/0004-637X/794/1/3](https://doi.org/10.1088/0004-637X/794/1/3)
- Virtanen, P., Gommers, R., Oliphant, T. E., et al. 2020, *Nature Methods*, 17, 261, doi: [10.1038/s41592-019-0686-2](https://doi.org/10.1038/s41592-019-0686-2)
- Wallerstein, G., & Sneden, C. 1982, *ApJ*, 255, 577, doi: [10.1086/159859](https://doi.org/10.1086/159859)
- Webbink, R. F. 1984, *ApJ*, 277, 355, doi: [10.1086/161701](https://doi.org/10.1086/161701)
- Wilson, E. C., & Nordhaus, J. 2019, *MNRAS*, 485, 4492, doi: [10.1093/mnras/stz601](https://doi.org/10.1093/mnras/stz601)
- . 2020, *MNRAS*, 497, 1895, doi: [10.1093/mnras/staa2088](https://doi.org/10.1093/mnras/staa2088)
- . 2022, *MNRAS*, 516, 2189, doi: [10.1093/mnras/stac2300](https://doi.org/10.1093/mnras/stac2300)
- Wolf, B., & Schwab, J. 2017, *wmwolf/py_mesa_reader: Interact with MESA Output, 0.3.0*, Zenodo, doi: [10.5281/zenodo.826958](https://doi.org/10.5281/zenodo.826958)
- Yamazaki, R., Hayasaki, K., & Loeb, A. 2017, *MNRAS*, 466, 1421, doi: [10.1093/mnras/stw3207](https://doi.org/10.1093/mnras/stw3207)
- Yan, H.-L., Shi, J.-R., Zhou, Y.-T., et al. 2018, *Nature Astronomy*, 2, 790, doi: [10.1038/s41550-018-0544-7](https://doi.org/10.1038/s41550-018-0544-7)
- Zhang, M., & Penev, K. 2014, *ApJ*, 787, 131, doi: [10.1088/0004-637X/787/2/131](https://doi.org/10.1088/0004-637X/787/2/131)
- Zhou, Y., Yan, H., Shi, J., et al. 2019, *ApJ*, 877, 104, doi: [10.3847/1538-4357/ab1b4b](https://doi.org/10.3847/1538-4357/ab1b4b)
- Zorotovic, M., & Schreiber, M. 2022, *MNRAS*, 513, 3587, doi: [10.1093/mnras/stac1137](https://doi.org/10.1093/mnras/stac1137)